Spectroelectrochemical investigations of nickel cyclam indicate different reaction mechanisms for electrocatalytic CO_2 and H^+ reduction

Shelby L. Behnke, Anastasia C. Manesis, Hannah S. Shafaat*

Supporting Information

Table of Contents

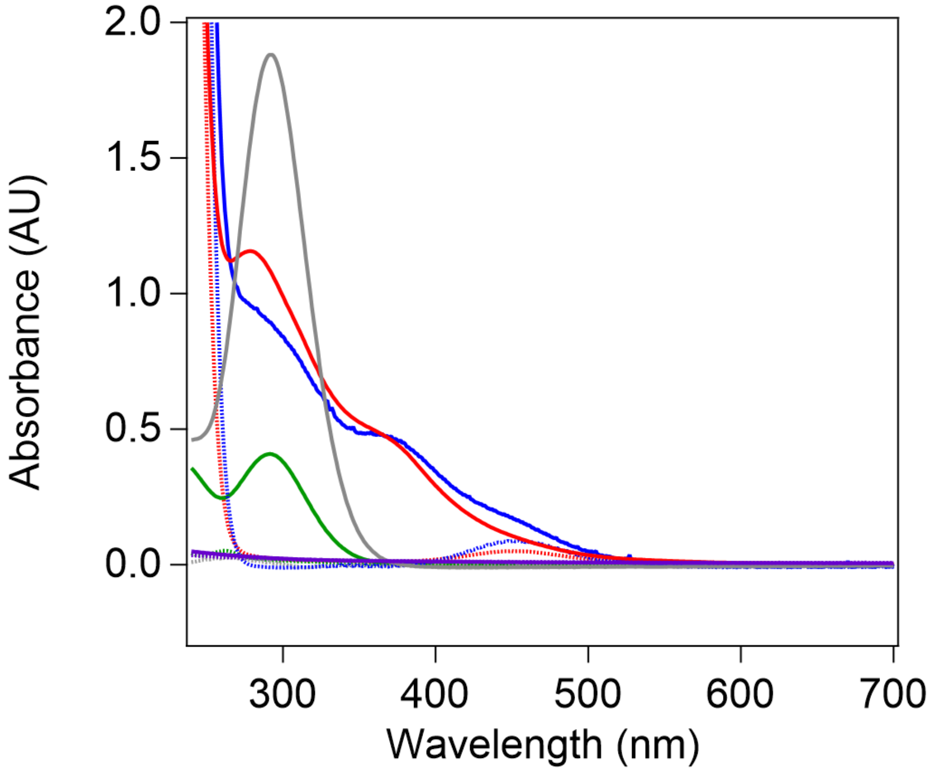

Figure S1. Optical absorption spectra of control samples. Optical absorption spectra of 1.2 mM [**1**] (red), buffer (grey), and $NiCl_2$ (green) prior to (dotted lines) or following (solid lines) 40 min of controlled potential electrolysis at -1.3 V vs. NHE. Also shown is the optical absorption spectrum of [**1**] after 40 min of controlled potential electrolysis at +1.2 V vs NHE (blue). All samples measured in 50 mM phosphate buffer, pH 7.0, 0.1 M KCl, under a saturating CO_2 atmosphere.

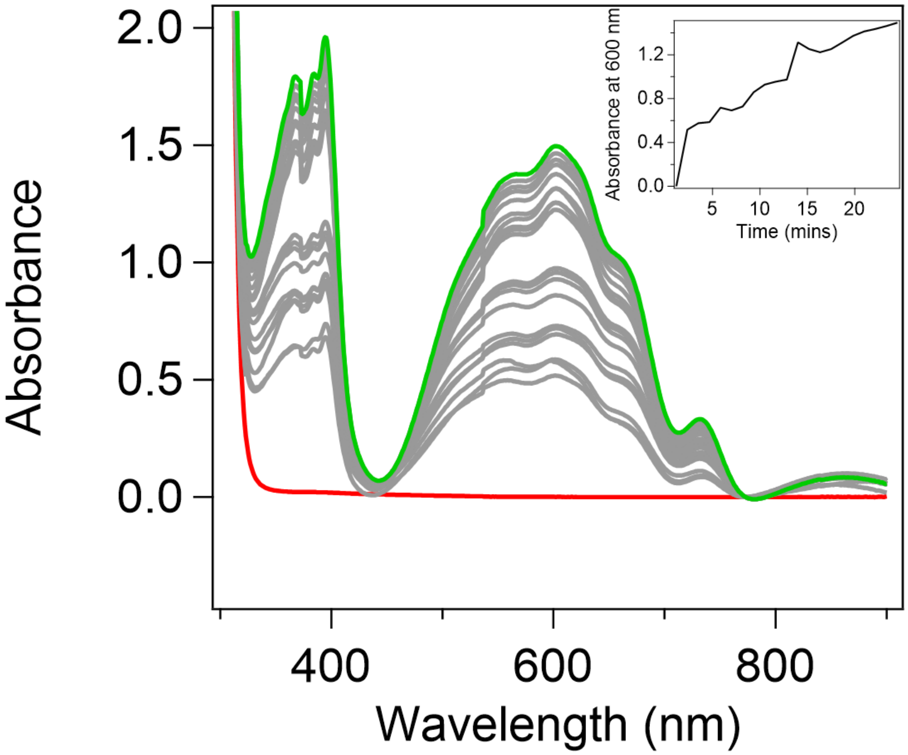

Figure S2. Optical spectroelectrochemical cell "leak test". Optical absorption spectra of 10 mM methyl viologen in 50 mM phosphate buffer, pH 7.0, with 0.1 M KCl prior to (red) and following (grey) 3 min. of controlled potential electrolysis at -1.3 V vs. NHE under an N_2 atmosphere. Also shown is the optical absorption spectrum of the same sample after sitting for 25 minutes with no potential applied (green). (*Inset*) Absorbance of the sample measured at 600 nm as a function of time during and following electrolysis.

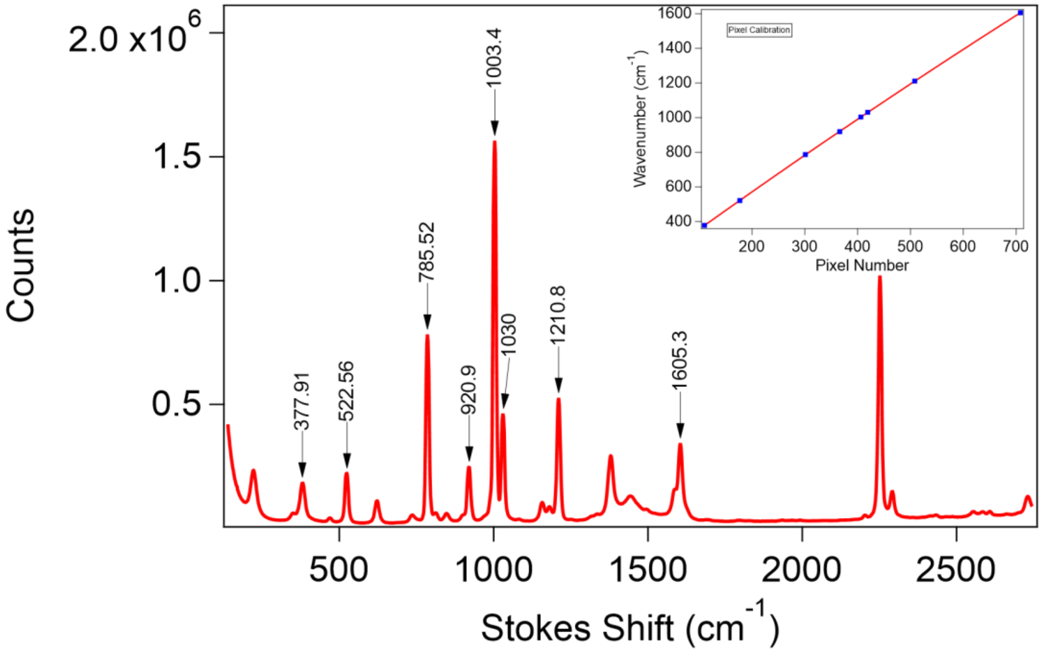

Figure S3. Resonance Raman calibration standard. Resonance Raman standard (1:1 acetonitrile:toluene) used for CCD pixel calibration. (*Inset*) Peak positions of the calibration standard as a function of pixel number.

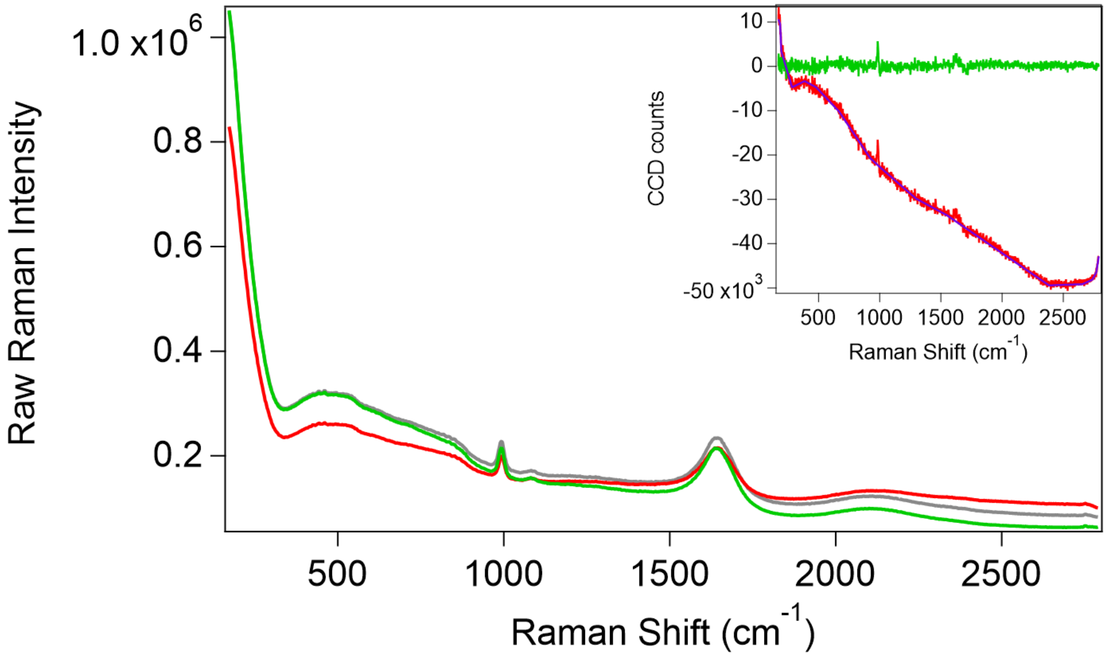

Figure S4. **Summed raw resonance Raman spectra of electrolyte control.** Summed raw resonance Raman spectra of 50 mM phosphate buffer, pH 7.0, with 0.1 M KCl under CO before (red), during (black) and after (green) 20 min. of electrolysis at -1.3 V vs. NHE (λ_{ex} = 364 nm, P = 20 mW, T = 298 K). (*Inset*) RR spectrum of electrolyzed solution prior to baseline correction generated by subtracting the summed spectrum obtained before electrolysis (red, main figure) from the spectrum obtained during electrolysis (grey, main figure) to fully remove features due to the 1600 cm^{-1} water band (red). A spline baseline (purple) was subtracted from the red trace to generate the final resonance Raman spectrum of the solution following electrolysis (green).

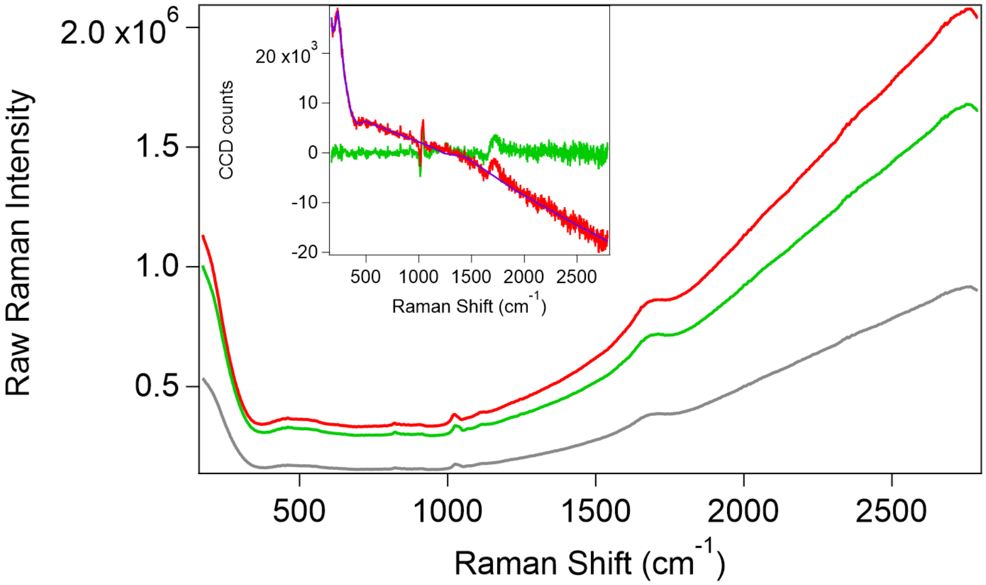

Figure S5. Summed raw resonance Raman spectra of nickel chloride control. Summed raw resonance Raman spectra of 1.2 mM $NiCl_2$, 50 mM phosphate buffer, pH 7.0, with 0.1 M KCl under CO before (red), during (black) and after (green) 20 min. of electrolysis at -1.3 V vs. NHE (λ_{ex} = 364 nm, P = 20 mW, T = 298 K). (*Inset*) RR spectrum of electrolyzed solution prior to baseline correction generated by subtracting the summed spectrum obtained before electrolysis (red, main figure) from the spectrum obtained during electrolysis (grey, main figure) to fully remove features due to the 1600 cm^{-1} water band (red). A spline baseline (purple) was subtracted from the red trace to generate the final resonance Raman spectrum of the solution following electrolysis (green).

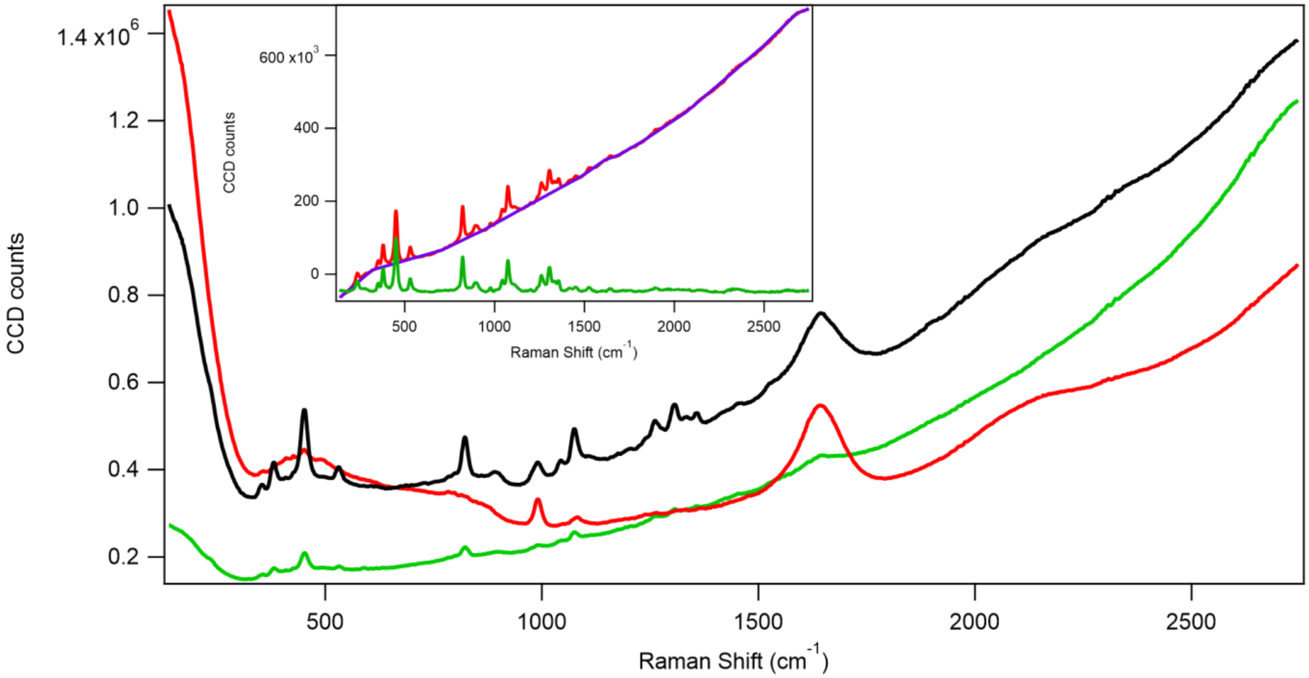

Figure S6. Raw Raman spectroelectrochemistry of [1] under N_2 atmosphere. Summed raw resonance Raman spectra of [**1**] in 50 mM phosphate buffer, pH 7.0, with 0.1 M KCl under N_2 before (red), during (black) and after (green) 20 min. of electrolysis at -1.3 V vs. NHE (λ_{ex} = 364 nm, P = 20 mW, T = 298 K). (*Inset*) RR spectrum of electrolyzed [**1**] prior to baseline correction generated by subtracting the summed spectrum obtained before electrolysis (red, main figure) from the spectrum obtained during electrolysis (black, main figure) to fully remove features due to the 1600 cm^{-1} water band (red). A spline baseline (purple) was subtracted from the red trace to generate the final resonance Raman spectrum of [**1**] following electrolysis (green; also shown in main text Figure 2B, black trace).

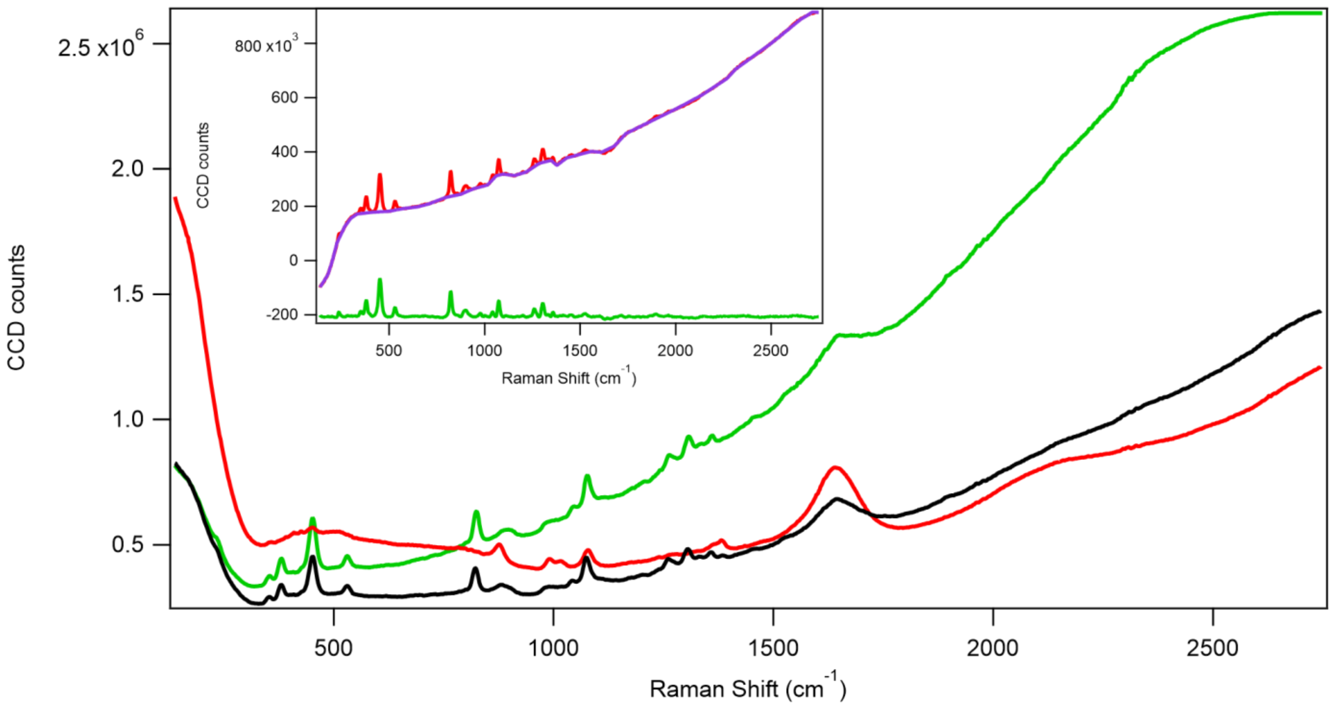

Figure S7. Raw resonance Raman spectroelectrochemistry of [1] under CO_2 atmosphere. Summed raw resonance Raman spectra of [**1**] in 50 mM phosphate buffer, pH 7.0, with 0.1 M KCl under CO_2 before (red), during (black) and after (green) 20 min. of electrolysis at -1.3 V vs. NHE (λ_{ex} = 364 nm, P = 20 mW, T = 298 K). (*Inset*) RR spectrum of electrolyzed [**1**] prior to baseline correction generated by subtracting the summed spectrum obtained before electrolysis (red, main figure) from the spectrum obtained during electrolysis (black, main figure) to fully remove features due to the 1600 cm^{-1} water band (red). A spline baseline (purple) was subtracted from the red trace to generate the final resonance Raman spectrum of [**1**] following electrolysis (green; also shown in main text Figure 2B, blue trace).

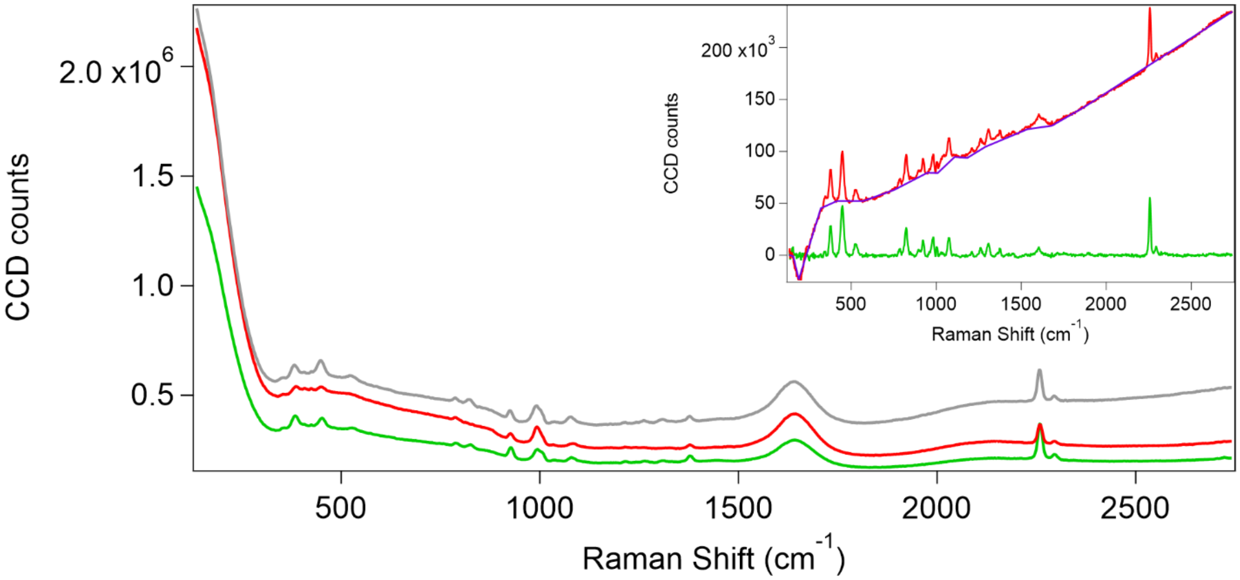

Figure S8. Raw Raman spectroelectrochemistry of [1] under CO atmosphere. Summed raw resonance Raman spectra of [**1**] in 50 mM phosphate buffer, pH 7.0, with 0.1 M KCl under CO before (red), during (black) and after (green) 20 min. of electrolysis at -1.3 V vs. NHE (λ_{ex} = 364 nm, P = 20 mW, T = 298 K). (*Inset*) RR spectrum of electrolyzed [**1**] prior to baseline correction generated by subtracting the summed spectrum obtained before electrolysis (red, main figure) from the spectrum obtained during electrolysis (grey, main figure) to fully remove features due to the 1600 cm^{-1} water band (red). A spline baseline (purple) was subtracted from the red trace to generate the final resonance Raman spectrum of [**1**] following electrolysis (green; also shown in main text Figure 2B, red trace).

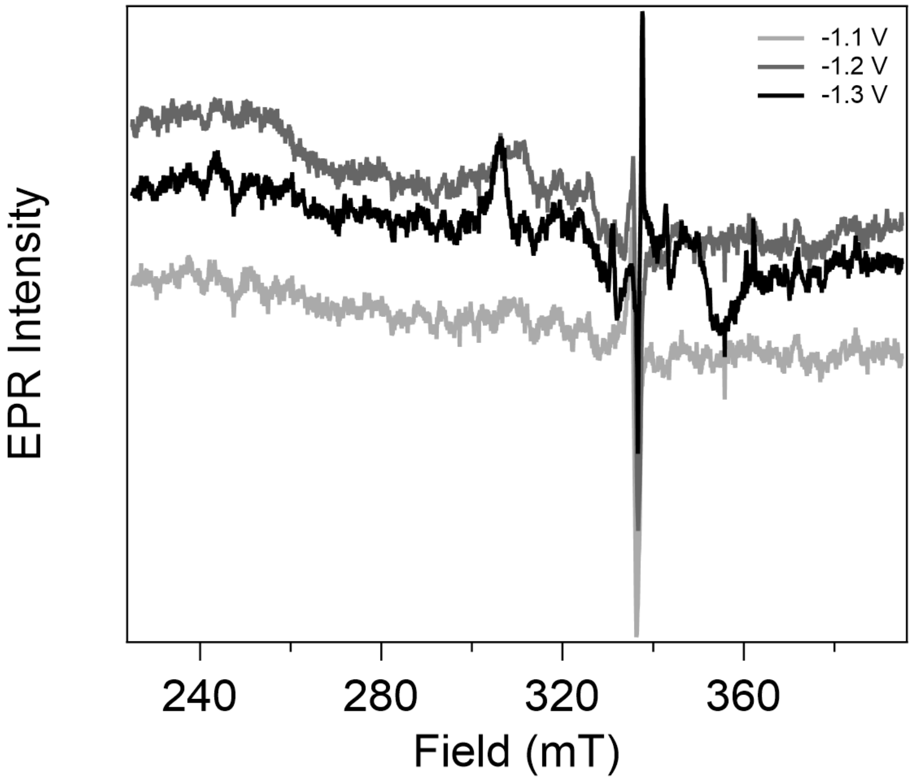

Figure S9. CW X-band EPR spectroelectrochemistry of free cyclam under a CO_2 atmosphere. CW X-band EPR spectra (T= 125 K, $P_{\mu w}$ = 20 mW, ν_{mw} = 9.4 GHz) of free cyclam ligand following 20 min. electrolysis at the indicated potentials (vs. NHE) using an AG rod working electrode. Samples were prepared in 50 mM phosphate buffer, pH 7.0, under a CO_2 atmosphere.

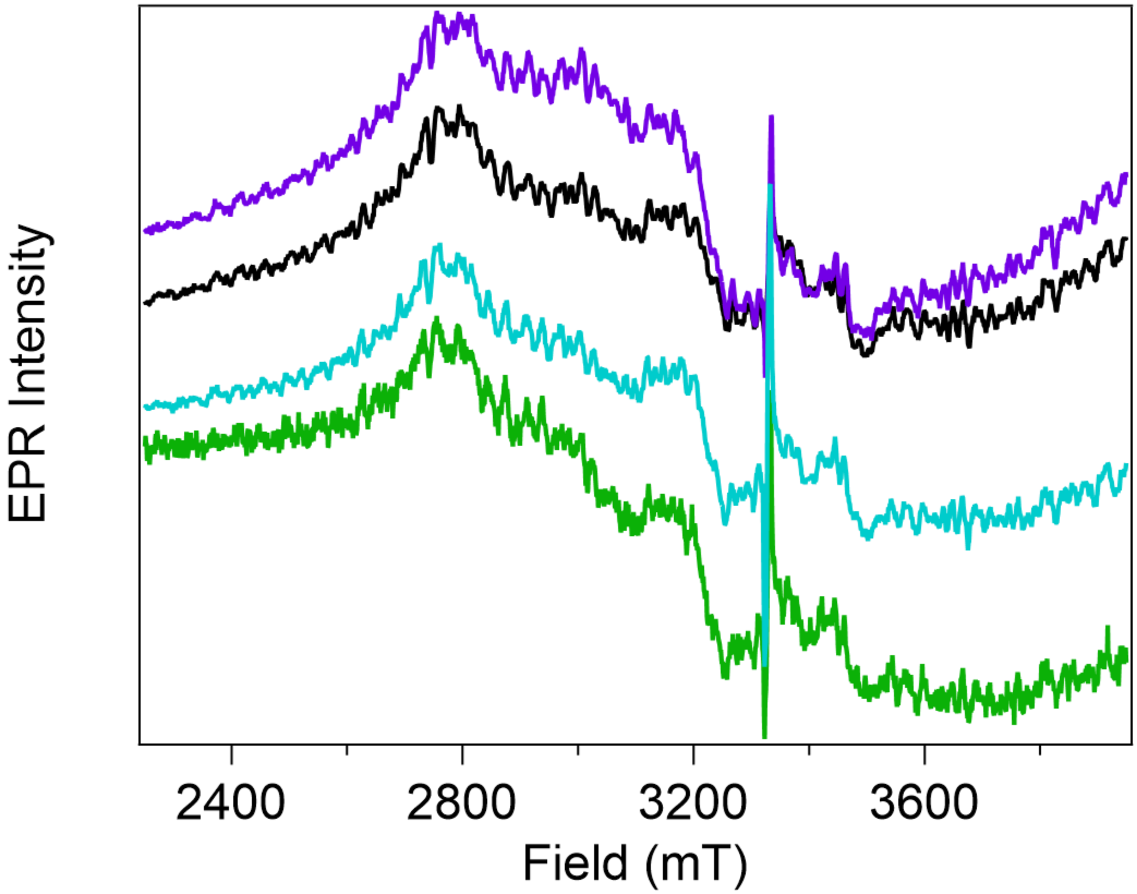

Figure S10. Control EPR spectroelectrochemistry experiments. CW X-band EPR spectra (T= 125 K, $P_{\mu w}$ = 20 mW, ν_{mw} = 9.4 GHz) of [**1**] under CO with no electrolysis (purple), $NiCl_2$*$6H_2O$ following 20 min. electrolysis at -1.3 V vs. NHE under a CO_2 atmosphere (black), $NiCl_2$*$6H_2O$ following 20 min. electrolysis at -1.3 V vs. NHE under an N_2 atmosphere (green), and $NiCl_2$*$6H_2O$ following 20 min. electrolysis at -1.3 V vs. NHE under a CO atmosphere (blue). Samples were prepared in 50 mM phosphate buffer at a final pH of 7.0, with 0.1 M KCl, and electrolysis was carried out using an AG rod.

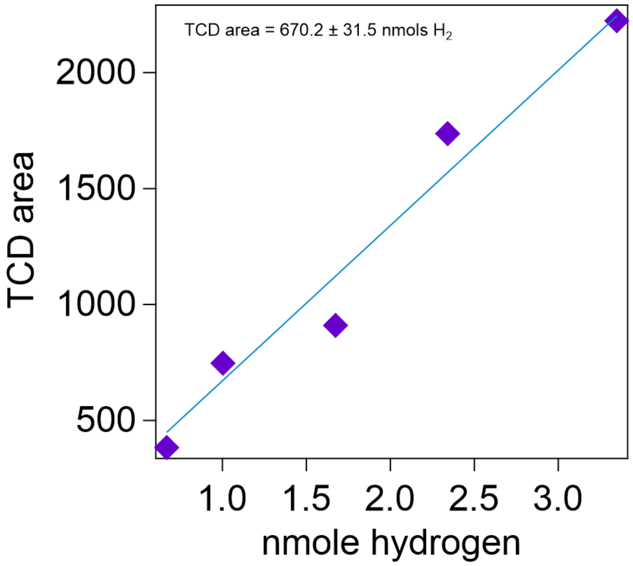

Figure S11. GCA calibration for hydrogen gas. Gas chromatography analysis calibration of H_2 TCD peak area with a known gas standard.

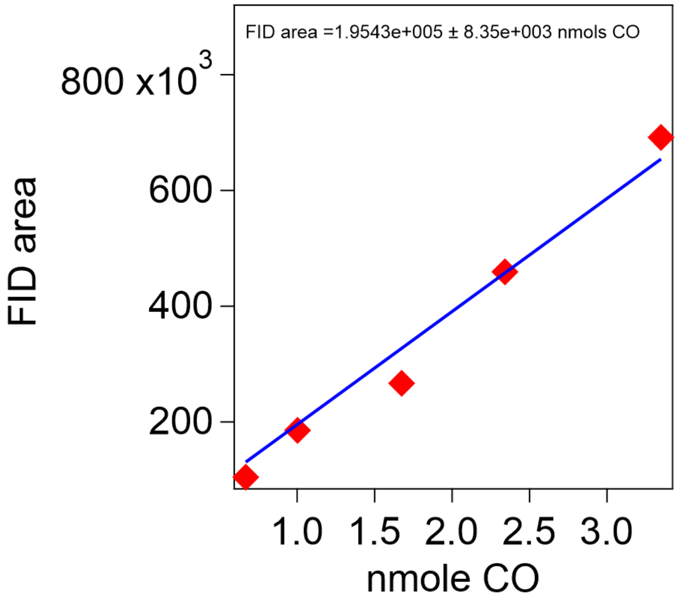

Figure S12. GCA calibration for carbon monoxide gas. Gas chromatography analysis calibration for CO FID peak area with a known gas standard.

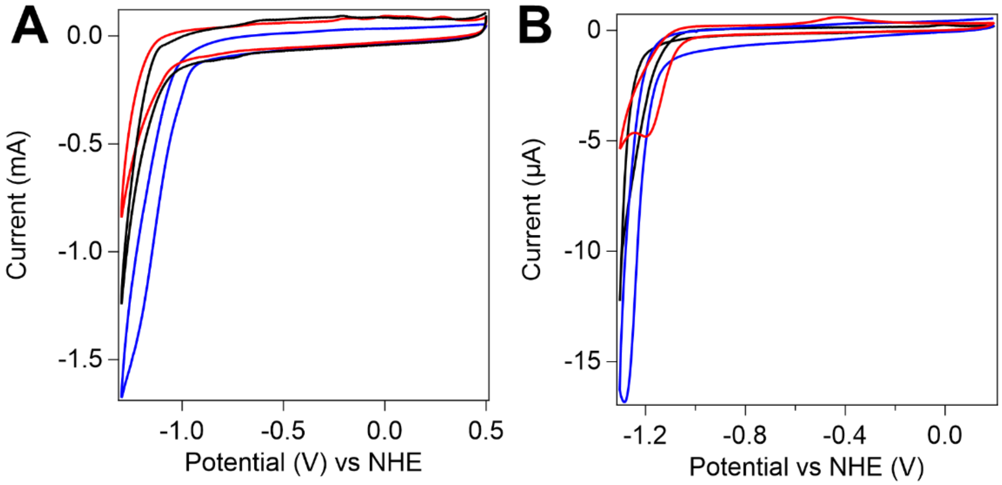

Figure S13. Cyclic voltammograms (CVs) of [1] with (A) AG and (B) GC working electrodes. CVs were run in 50 mM phosphate buffer, pH 7.0, with 0.1 M KCl under an atmosphere of N_2 (black), CO_2 (blue), and CO (red) (ν = 10 mV/s).

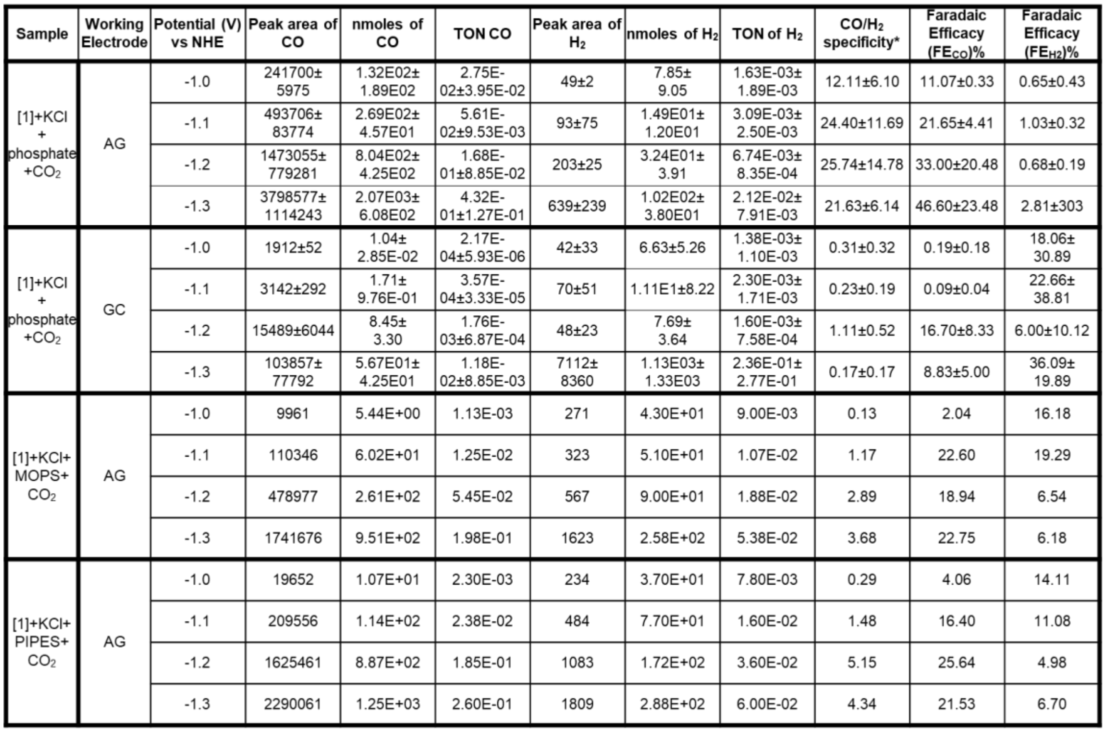

Sample	Working Electrode	Potential (V) vs NHE	Peak area of CO	nmoles of CO	TON CO	Peak area of H_2	nmoles of H_2	TON of H_2	CO/H_2 specificity*	Faradaic Efficacy (FE_{CO})%	Faradaic Efficacy (FE_{H2})%
[1]+KCl + phosphate +CO_2	AG	-1.0	241700±5975	1.32E02±1.89E02	2.75E-02±3.95E-02	49±2	7.85±9.05	1.63E-03±1.89E-03	12.11±6.10	11.07±0.33	0.65±0.43
		-1.1	493706±83774	2.69E02±4.57E01	5.61E-02±9.53E-03	93±75	1.49E01±1.20E01	3.09E-03±2.50E-03	24.40±11.69	21.65±4.41	1.03±0.32
		-1.2	1473055±779281	8.04E02±4.25E02	1.68E-01±8.85E-02	203±25	3.24E01±3.91	6.74E-03±8.35E-04	25.74±14.78	33.00±20.48	0.68±0.19
		-1.3	3798577±1114243	2.07E03±6.08E02	4.32E-01±1.27E-01	639±239	1.02E02±3.80E01	2.12E-02±7.91E-03	21.63±6.14	46.60±23.48	2.81±303
[1]+KCl + phosphate +CO_2	GC	-1.0	1912±52	1.04±2.85E-02	2.17E-04±5.93E-06	42±33	6.63±5.26	1.38E-03±1.10E-03	0.31±0.32	0.19±0.18	18.06±30.89
		-1.1	3142±292	1.71±9.76E-01	3.57E-04±3.33E-05	70±51	1.11E1±8.22	2.30E-03±1.71E-03	0.23±0.19	0.09±0.04	22.66±38.81
		-1.2	15489±6044	8.45±3.30	1.76E-03±6.87E-04	48±23	7.69±3.64	1.60E-03±7.58E-04	1.11±0.52	16.70±8.33	6.00±10.12
		-1.3	103857±77792	5.67E01±4.25E01	1.18E-02±8.85E-03	7112±8360	1.13E03±1.33E03	2.36E-01±2.77E-01	0.17±0.17	8.83±5.00	36.09±19.89
[1]+KCl+ MOPS+ CO_2	AG	-1.0	9961	5.44E+00	1.13E-03	271	4.30E+01	9.00E-03	0.13	2.04	16.18
		-1.1	110346	6.02E+01	1.25E-02	323	5.10E+01	1.07E-02	1.17	22.60	19.29
		-1.2	478977	2.61E+02	5.45E-02	567	9.00E+01	1.88E-02	2.89	18.94	6.54
		-1.3	1741676	9.51E+02	1.98E-01	1623	2.58E+02	5.38E-02	3.68	22.75	6.18
[1]+KCl+ PIPES+ CO_2	AG	-1.0	19652	1.07E+01	2.30E-03	234	3.70E+01	7.80E-03	0.29	4.06	14.11
		-1.1	209556	1.14E+02	2.38E-02	484	7.70E+01	1.60E-02	1.48	16.40	11.08
		-1.2	1625461	8.87E+02	1.85E-01	1083	1.72E+02	3.60E-02	5.15	25.64	4.98
		-1.3	2290061	1.25E+03	2.60E-01	1809	2.88E+02	6.00E-02	4.34	21.53	6.70

*Average specificity was given as the mean of the specificity ratios derived from individual experiments, i.e., $\frac{1}{n}\sum_{i=1}^{n}\frac{nmoles\ CO,i}{nmoles\ H_2,i}$

Table ST1. GCA results for electrolysis of [1] under a CO_2 atmosphere. Compiled gas chromatography data for electrolysis products of 1.2 mM [**1**] in 50 mM buffer (buffer as indicated), pH 7.0, with 0.1 M KCl. Electrolysis was performed in a 20 mL gas-tight vial with 4 mL of solution. 150 µL injections were performed from a gas-tight syringe. When indicated, error reflects the standard deviation from n=3 independent experiments.

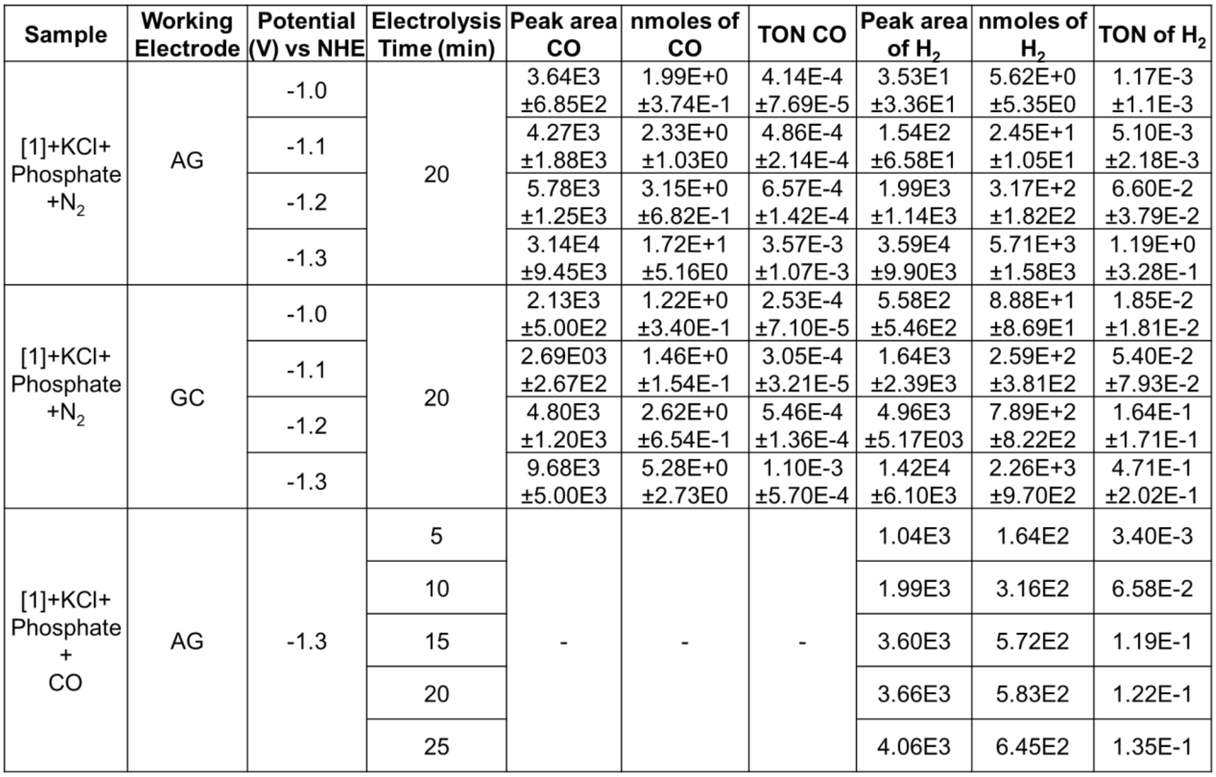

Sample	Working Electrode	Potential (V) vs NHE	Electrolysis Time (min)	Peak area CO	nmoles of CO	TON CO	Peak area of H_2	nmoles of H_2	TON of H_2
[1]+KCl+ Phosphate +N_2	AG	-1.0	20	3.64E3 ±6.85E2	1.99E+0 ±3.74E-1	4.14E-4 ±7.69E-5	3.53E1 ±3.36E1	5.62E+0 ±5.35E0	1.17E-3 ±1.1E-3
		-1.1		4.27E3 ±1.88E3	2.33E+0 ±1.03E0	4.86E-4 ±2.14E-4	1.54E2 ±6.58E1	2.45E+1 ±1.05E1	5.10E-3 ±2.18E-3
		-1.2		5.78E3 ±1.25E3	3.15E+0 ±6.82E-1	6.57E-4 ±1.42E-4	1.99E3 ±1.14E3	3.17E+2 ±1.82E2	6.60E-2 ±3.79E-2
		-1.3		3.14E4 ±9.45E3	1.72E+1 ±5.16E0	3.57E-3 ±1.07E-3	3.59E4 ±9.90E3	5.71E+3 ±1.58E3	1.19E+0 ±3.28E-1
[1]+KCl+ Phosphate +N_2	GC	-1.0	20	2.13E3 ±5.00E2	1.22E+0 ±3.40E-1	2.53E-4 ±7.10E-5	5.58E2 ±5.46E2	8.88E+1 ±8.69E1	1.85E-2 ±1.81E-2
		-1.1		2.69E03 ±2.67E2	1.46E+0 ±1.54E-1	3.05E-4 ±3.21E-5	1.64E3 ±2.39E3	2.59E+2 ±3.81E2	5.40E-2 ±7.93E-2
		-1.2		4.80E3 ±1.20E3	2.62E+0 ±6.54E-1	5.46E-4 ±1.36E-4	4.96E3 ±5.17E03	7.89E+2 ±8.22E2	1.64E-1 ±1.71E-1
		-1.3		9.68E3 ±5.00E3	5.28E+0 ±2.73E0	1.10E-3 ±5.70E-4	1.42E4 ±6.10E3	2.26E+3 ±9.70E2	4.71E-1 ±2.02E-1
[1]+KCl+ Phosphate + CO	AG	-1.3	5	-	-	-	1.04E3	1.64E2	3.40E-3
			10				1.99E3	3.16E2	6.58E-2
			15				3.60E3	5.72E2	1.19E-1
			20				3.66E3	5.83E2	1.22E-1
			25				4.06E3	6.45E2	1.35E-1

Table ST2. GCA results for electrolysis of [1] under an N_2 or CO atmosphere. Compiled gas chromatography data for electrolysis products of 1.2 mM [**1**] in 50 mM phosphate buffer, pH 7.0, with 0.1 M KCl. Electrolysis was performed in a 20 mL gas-tight vial with 4 mL of solution. 150 µL injections were performed from a gas-tight syringe. When indicated, error reflects the standard deviation from n=3 independent experiments.

Compound	**Potential (V) vs NHE**	**CO peak area**	**nmoles of CO**	**TON of CO**	**H_2 peak area**	**nmoles of H_2**	**TON H_2**
cyclam+KCl +Phosphate +CO_2	-1.0	7040	3.84E+00	8.01E-04	749	1.19E+02	2.48E-02
	-1.1	19434	1.06E+01	2.21E-03	1083	1.72E+02	3.59E-02
	-1.2	38573	2.11E+01	4.39E-03	2143	3.41E+02	7.11E-02
	-1.3	108011	5.90E+01	1.23E-02	4590	7.31E+02	1.52E-01
KCl+ Phosphate+ CO_2	-1.0	0	-	-	1548	2.46E+02	-
	-1.1	0	-	-	3572	5.68E+02	-
	-1.2	0	-	-	4763	7.58E+02	-
	-1.3	51	2.78E-02	-	16569	2.64E+03	-

Table ST3. GCA results for electrolysis of control experiments under a CO_2 atmosphere. Compiled gas chromatography data for electrolysis products of 1.2 mM free cyclam ligand or electrolyte alone, as indicated, in 50 mM phosphate buffer, pH 7.0, with 0.1 M KCl. Electrolysis was performed in a 20 mL gas-tight vial with 4 mL of solution. 150 µL injections were performed from a gas-tight syringe. When indicated, error reflects the standard deviation from n=3 independent experiments.

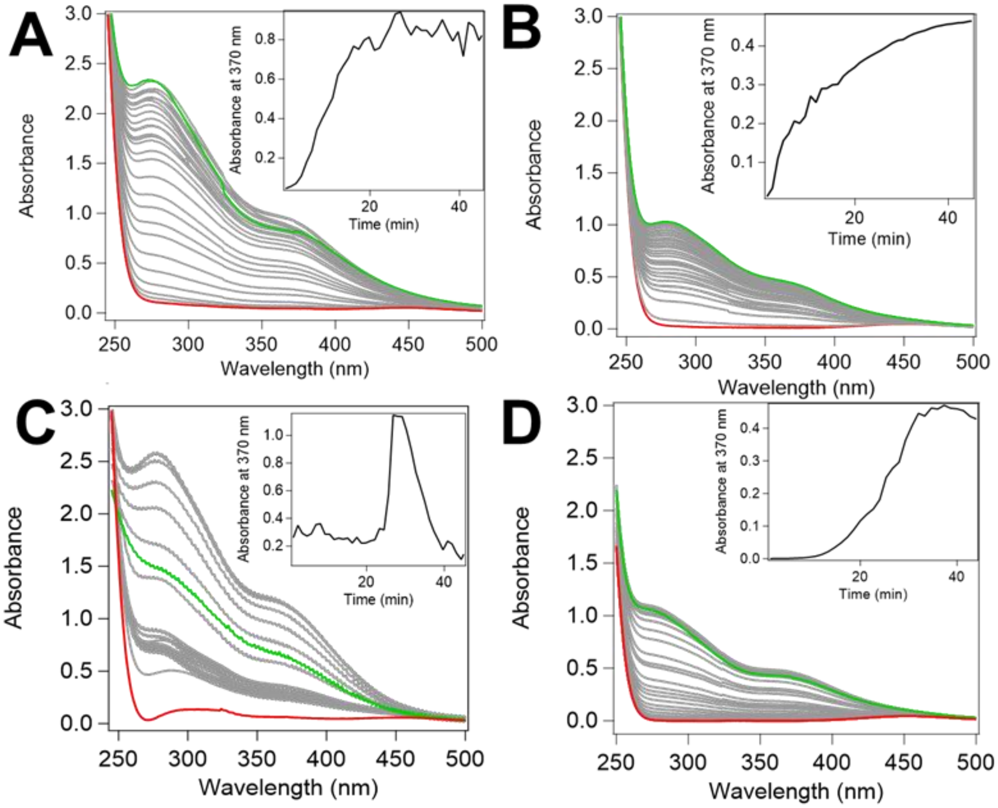

Figure S14. Reductive spectroelectrochemistry of [1] under various gases. Spectroelectrochemistry of 1.2 mM [**1**] under saturating (A) N_2, (B) CO_2, (C) CO, and (D) air atmospheres. Samples contained 0.1 M KCl in a 50 mM phosphate buffer, pH 7.0. Samples were electrolyzed at -1.3 V vs NHE using an amorphous graphite rod as the working electrode. Spectra highlighted were taken at t = 1 min (red) and t = 45 min (green). (*Insets*) Absorbance values at 370 nm measured as a function of electrolysis time.

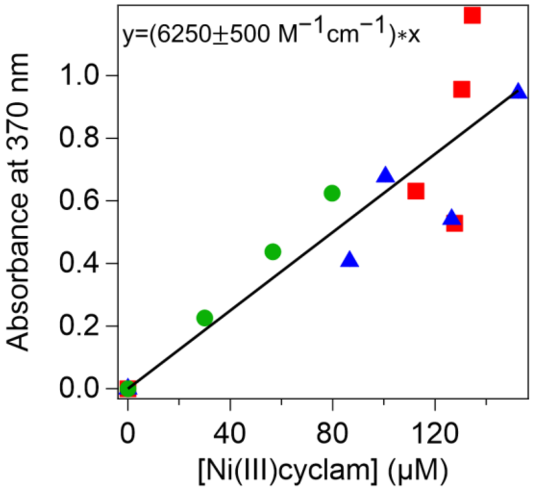

Figure S15. Extinction coefficient determination for the EPR-active species. Optical spectroelectrochemistry of a 1.2 mM solution of [**1**] under a CO_2 atmosphere. Samples contained 0.1 M KCl in a 50 mM phosphate buffer, pH 7.0. Samples were electrolyzed at -1.3 V (red squares and blue triangles) vs. NHE or +1.2 V (green circles) vs. NHE using an amorphous graphite rod as the working electrode. A linear fit to the data (black line) was used to determine the extinction coefficient.

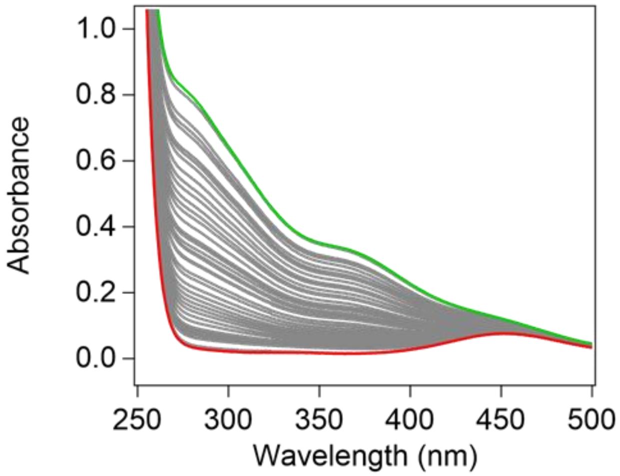

Figure S16. Reductive spectroelectrochemistry of [1] using a GC working electrode. Spectroelectrochemistry of 1.2 mM [**1**] under a CO_2 atmosphere. Sample contained 0.1 M KCl in a 50 mM phosphate buffer, pH 7.0 and was electrolyzed at -1.3 V vs NHE using an amorphous glassy carbon rod as the working electrode. Spectra were taken at t = 1 min (red), t = 2 – 44 min (grey), and t = 45 min (green).

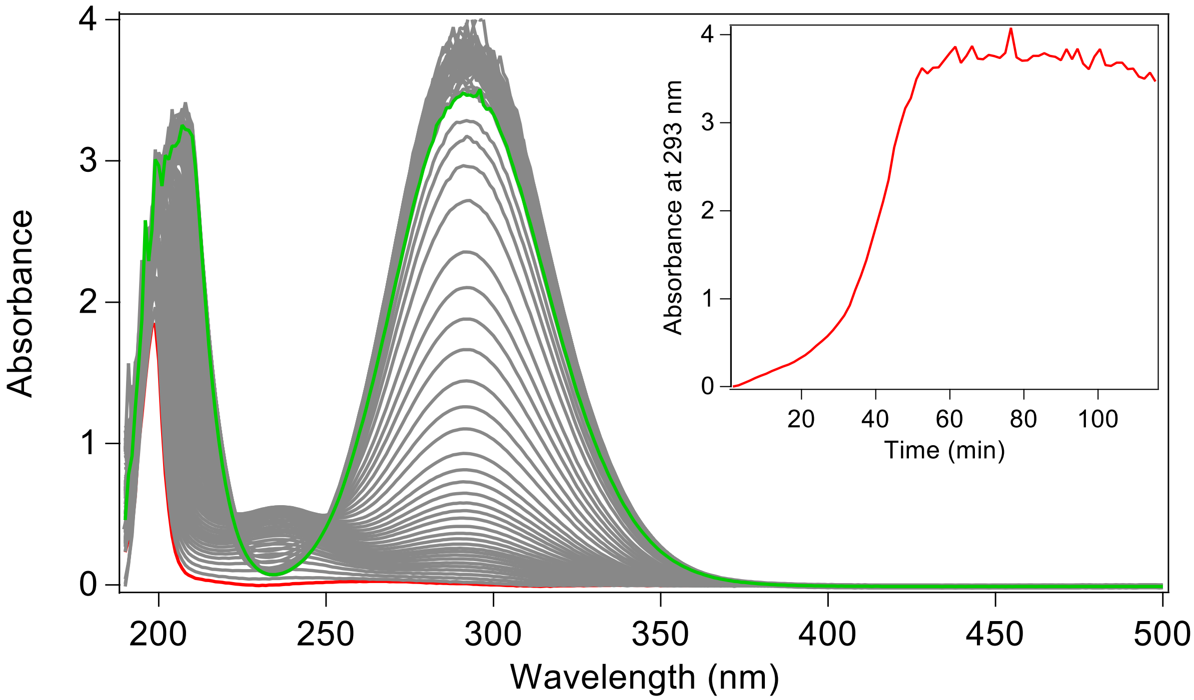

Figure S17. Degradation of electrolyte after extended electrolysis. Optical spectroelectrochemistry of electrolyte-only control under a CO_2 atmosphere. Sample contained 0.1 M KCl in a 50 mM phosphate buffer, pH 7.0. Sample was electrolyzed at -1.3 V vs NHE using an amorphous graphite rod as the working electrode. Spectra highlighted were taken at t = 1 min (red) and t = 120 min (green). (*Inset*) Absorbance at 293 nm followed as a function of electrolysis time.

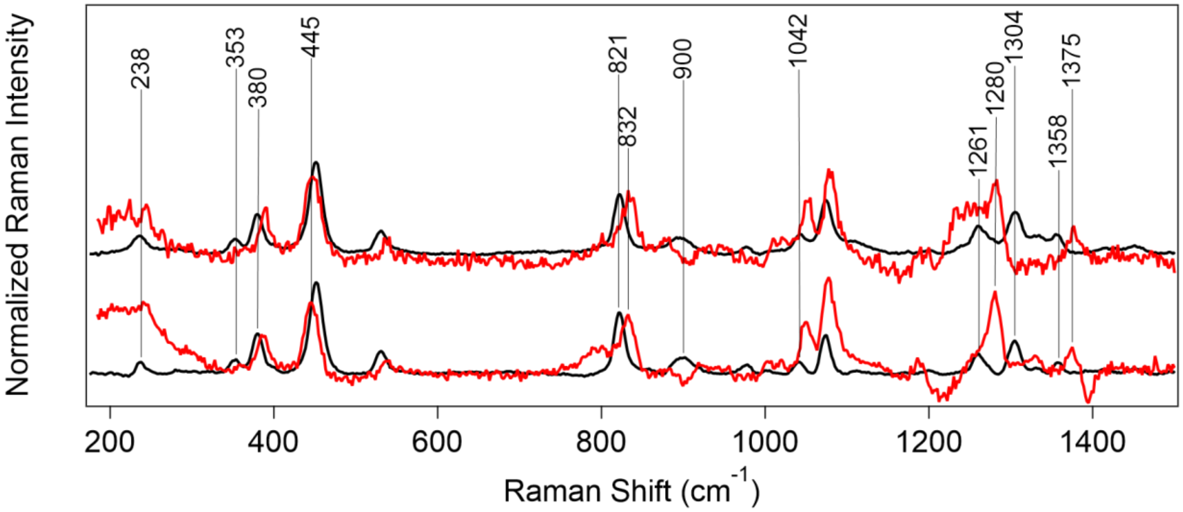

Figure S18. Reductive resonance Raman spectroelectrochemistry of [1] in H_2O and D_2O under N_2 and CO_2 atmospheres. Normalized resonance Raman spectra (λ_{ex} = 364 nm, P = 20 mW, T = 298 K) of [**1**] in H_2O (black) and D_2O (red) buffers (50 mM phosphate, pL = 7.0, 0.1 M KCl) following electrolysis at -1.3 V vs. NHE under N_2 and CO_2, as labeled. Electrolysis was performed using an AG working electrode.

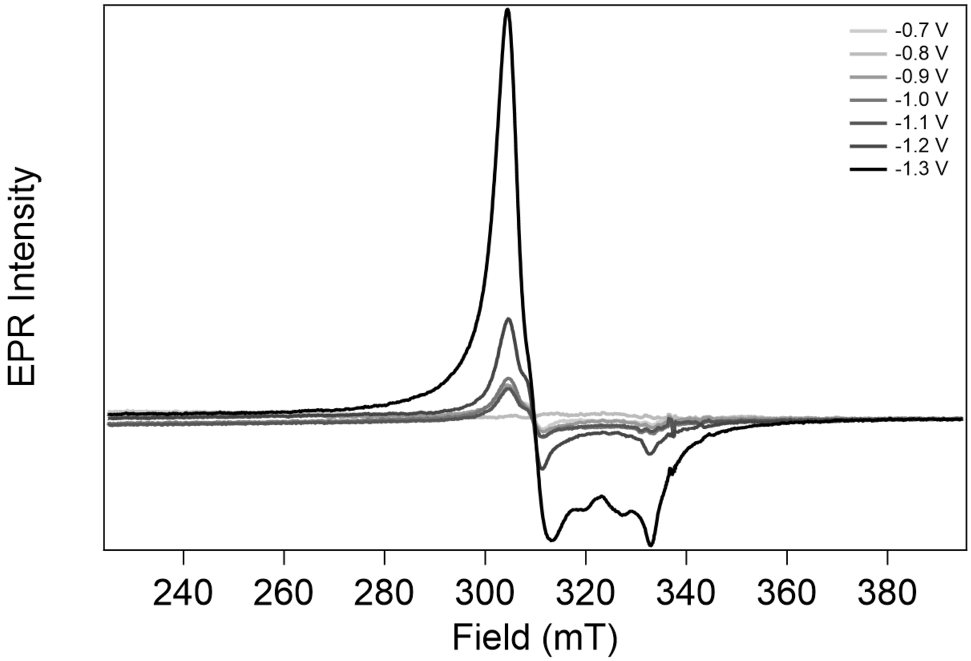

Figure S19. CW X-band EPR spectroelectrochemistry of [1] under an N_2 atmosphere. CW X-band EPR spectra (T= 100 K, $P_{\mu w}$ = 20 mW, ν_{mw} = 9.4 GHz) of [**1**] following 20 min. electrolysis at the indicated potentials (vs. NHE) using an AG rod working electrode. Samples were prepared in 50 mM phosphate buffer, pH 7.0, under an N_2 atmosphere.

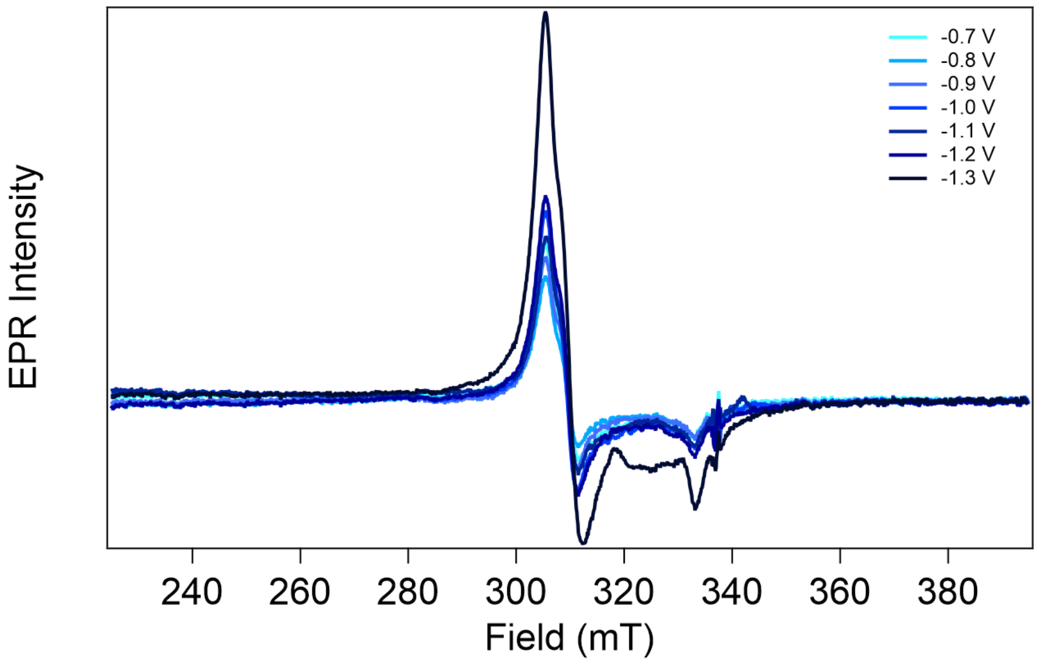

Figure S20. CW X-band EPR spectroelectrochemistry of [1] under a CO_2 atmosphere. CW X-band EPR spectra (T= 100 K, $P_{\mu w}$ = 20 mW, ν_{mw} = 9.4 GHz) of [**1**] following 20 min. electrolysis at the indicated potentials (vs. NHE) using an AG rod working electrode. Samples were prepared in 50 mM phosphate buffer, pH 7.0, under a CO_2 atmosphere.

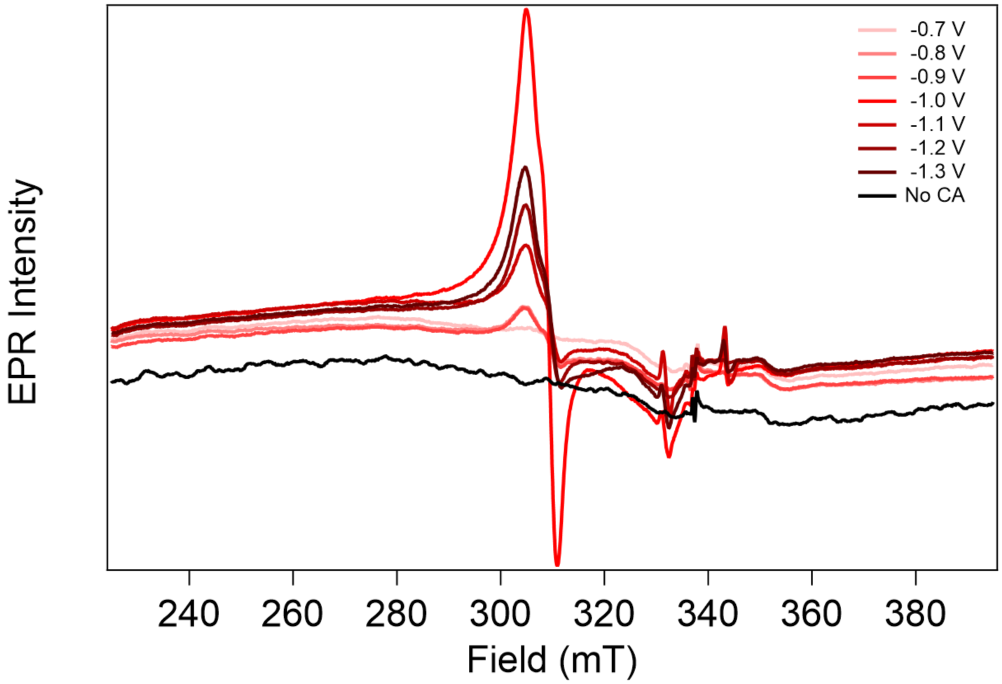

Figure S21. CW X-band EPR spectroelectrochemistry of [1] under a CO atmosphere. CW X-band EPR spectra (T= 100 K, $P_{\mu w}$ = 20 mW, ν_{mw} = 9.4 GHz) of [**1**] following 20 min. electrolysis at the indicated potentials (vs. NHE) using an AG rod working electrode. Samples were prepared in 50 mM phosphate buffer, pH 7.0, under a CO atmosphere. Black trace labeled "No CA" represents a sample measured prior to electrolysis.

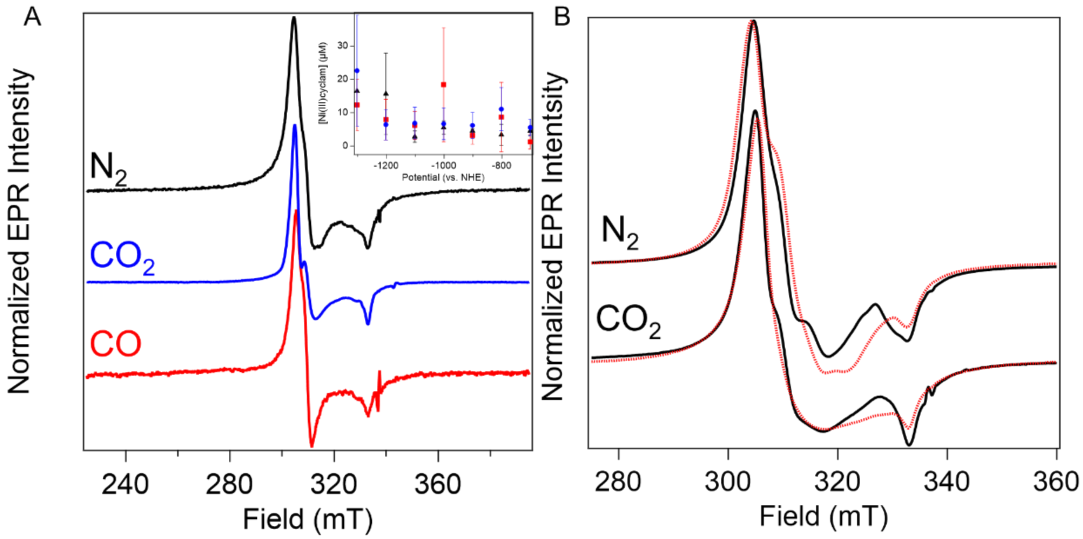

Figure S22. CW X-band EPR spectroelectrochemistry of [1] under various atmospheres. (A) Normalized CW X-band EPR spectra (T= 100 K, $P_{\mu w}$ = 20 mW, ν_{mw} = 9.4 GHz) of [**1**] following 20 min. electrolysis at -1.2 V vs. NHE under N_2 (black), CO_2 (blue), and CO (red) in 50 mM phosphate buffer, pH 7.0, with 0.1 M KCl. (*Inset*) Potential dependence of $[Ni(cyclam)]^{3+}$ generated by electrolysis under N_2 (black triangles), CO_2 (blue circles), and CO (red squares). (B) Normalized CW X-band EPR spectra (T= 100 K, $P_{\mu w}$ = 20 mW) of [**1**] following 20 min. electrolysis at -1.3 V vs. NHE under N_2 and CO_2 as indicated in H_2O (black) and D_2O (red) buffers (50 mM phosphate buffer, pL 7.0, with 0.1 M KCl).

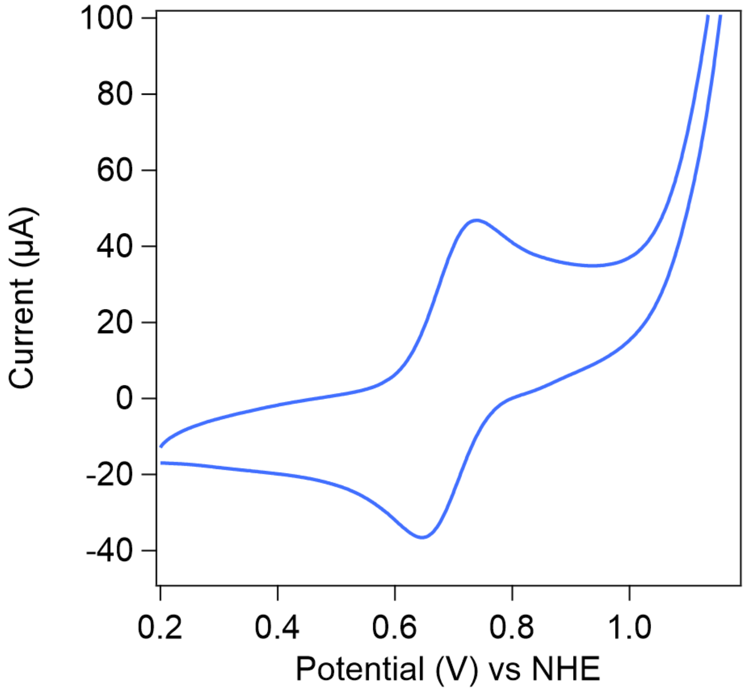

Figure S23. Cyclic voltammetry of [1] at oxidizing potentials. Cyclic voltammogram (CV) of [**1**] under an atmosphere of CO_2 (ν = 10 mV/s). CV was run with an amorphous graphite working electrode in 50 mM phosphate buffer, pH 7.0, with 0.1 M KCl.

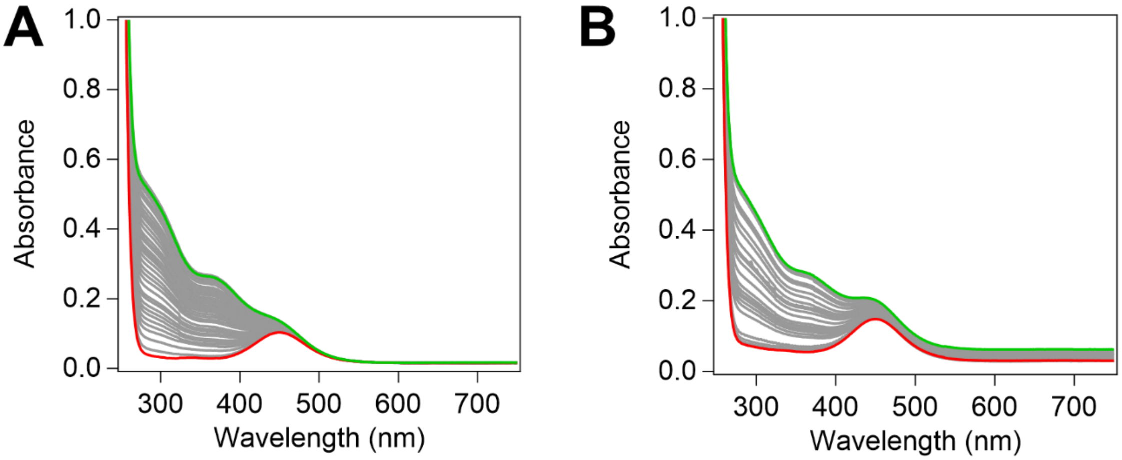

Figure S24. Oxidative spectroelectrochemistry of [1] under N_2 and CO_2 atmospheres. Spectroelectrochemistry of 1.2 mM [**1**] (A) under N_2 and (B) under CO_2 atmospheres. Samples contained 0.1 M $NaClO_4$ and 50 mM phosphate buffer, pH 7.0. Samples were electrolyzed at +1.2 V vs NHE using an amorphous graphite rod as a working electrode. Spectra highlighted were taken at t = 1 min (red) and t = 40 min (green).

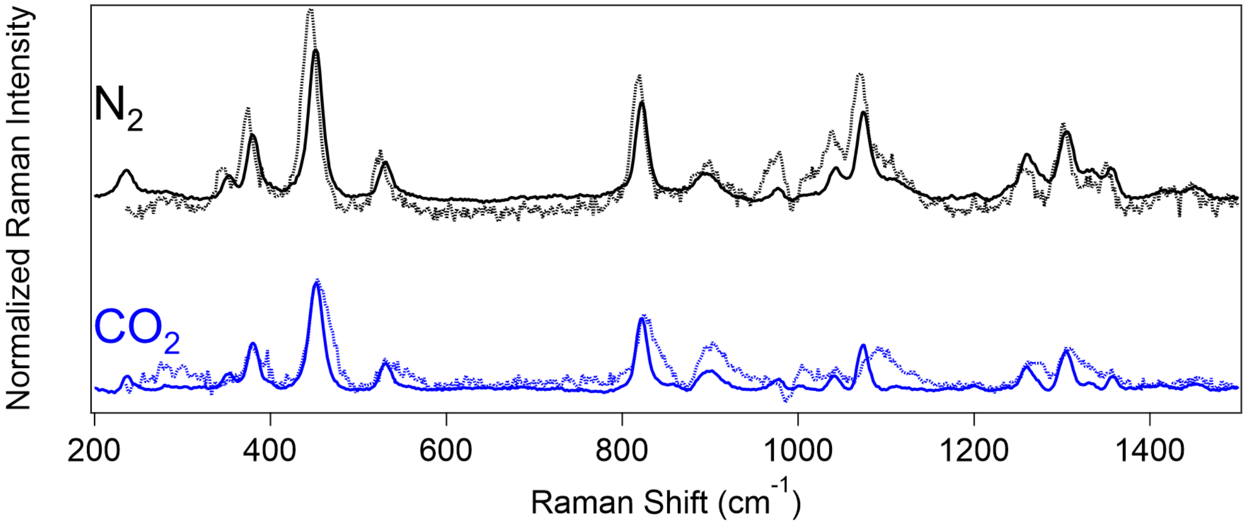

Figure S25. Reductive and oxidative resonance Raman spectroelectrochemistry of [1] under N_2 and CO_2 atmospheres. Normalized resonance Raman spectra (λ_{ex} = 364 nm, P = 20 mW, T = 298 K) of [**1**] in H_2O buffers following electrolysis at -1.3 V vs. NHE (solid lines) and +1.2 V vs. NHE (dotted lines) under N_2 (black) and CO_2 (blue). Electrolysis was performed using an AG working electrode.

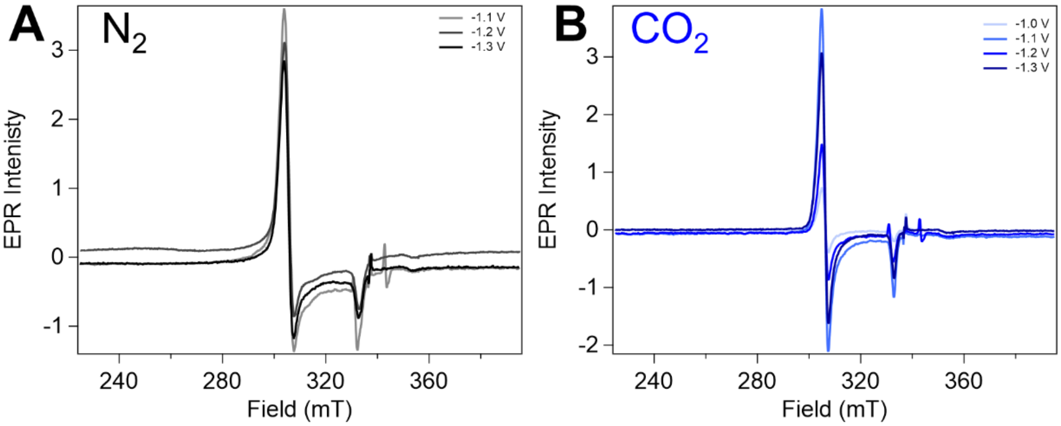

Figure S26. CW X-band EPR spectroelectrochemistry of [2] under N_2 and CO_2 atmospheres using a GC working electrode. (A) CW X-band EPR spectra (T= 125 K, $P_{\mu w}$ = 20 mW, ν_{mw} = 9.4 GHz) of [**2**] following 20 min. electrolysis at the indicated potentials under (A) N_2 and (B) CO_2 in 50 mM phosphate buffer, pH 7.0, with 0.1 M $NaClO_4$ using a GC rod working electrode.

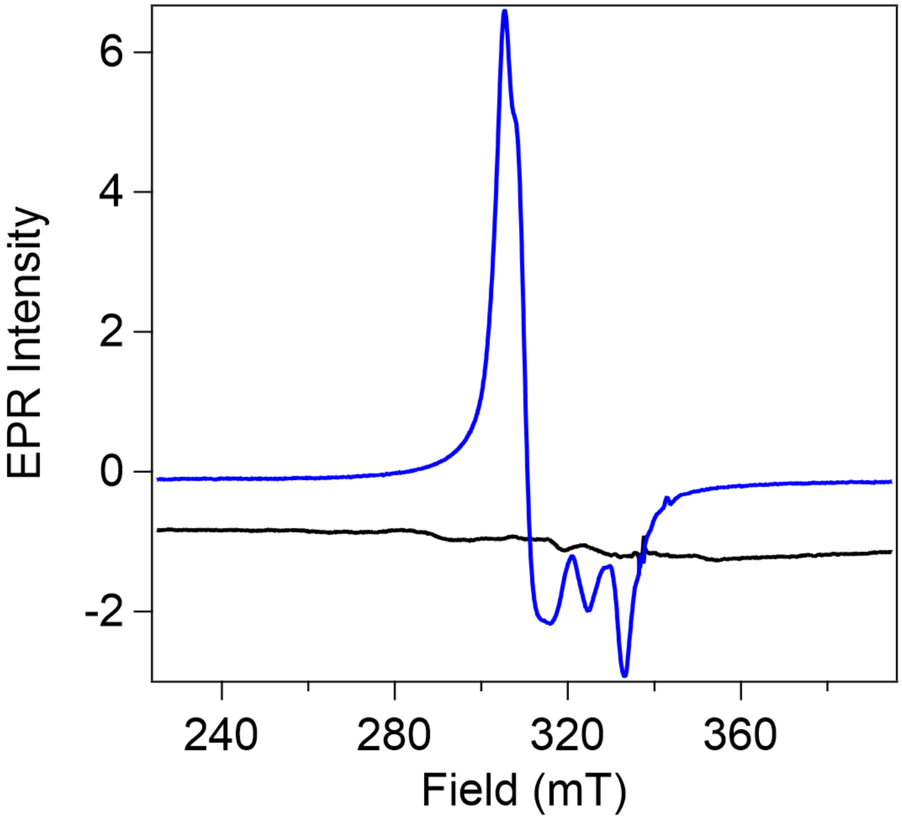

Figure S27. CW X-band EPR spectroelectrochemistry of [1] with the addition of dithionite. CW X-band EPR spectra (T= 100 K, $P_{\mu w}$ = 20 mW) of [**1**] following 20 min. electrolysis under CO_2 in 50 mM phosphate buffer, pH 7.0, with 0.1 M KCl. Sample was electrolyzed at -1.3 V vs. NHE (blue). Following electrolysis, 40 mM dithionite was added to the sample of electrolyzed [**1**] (black).

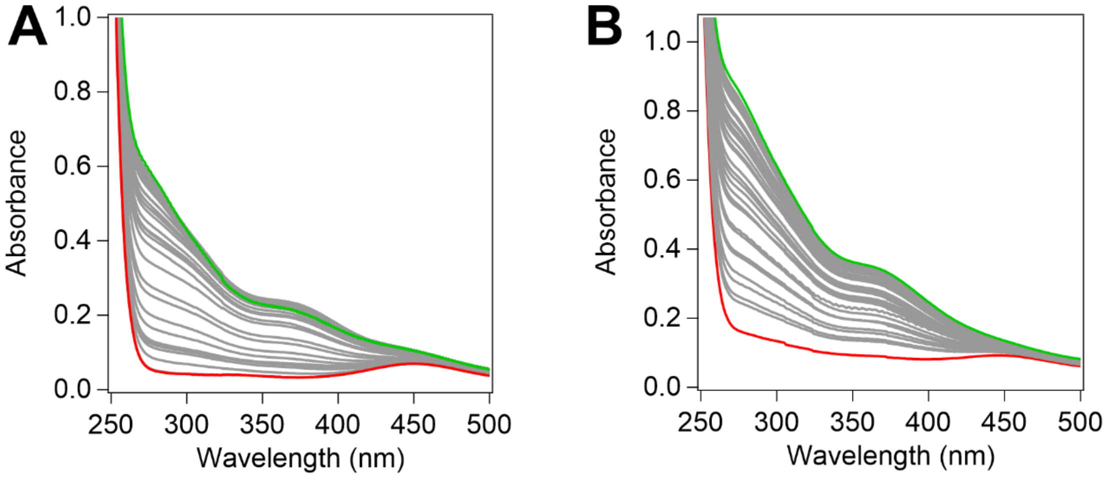

Figure S28. Reductive spectroelectrochemistry of [2] under N_2 and CO_2 atmospheres. Spectroelectrochemistry of 1.2 mM [**2**] (A) under N_2 and (B) under CO_2 atmospheres. Samples contained 0.1 M $NaClO_4$ in a 50 mM phosphate buffer, pH 7.0. Samples were electrolyzed at -1.3 V vs NHE using an amorphous graphite rod as the working electrode. Spectra highlighted were taken at t = 1 min (red) and t = 120 min (green).

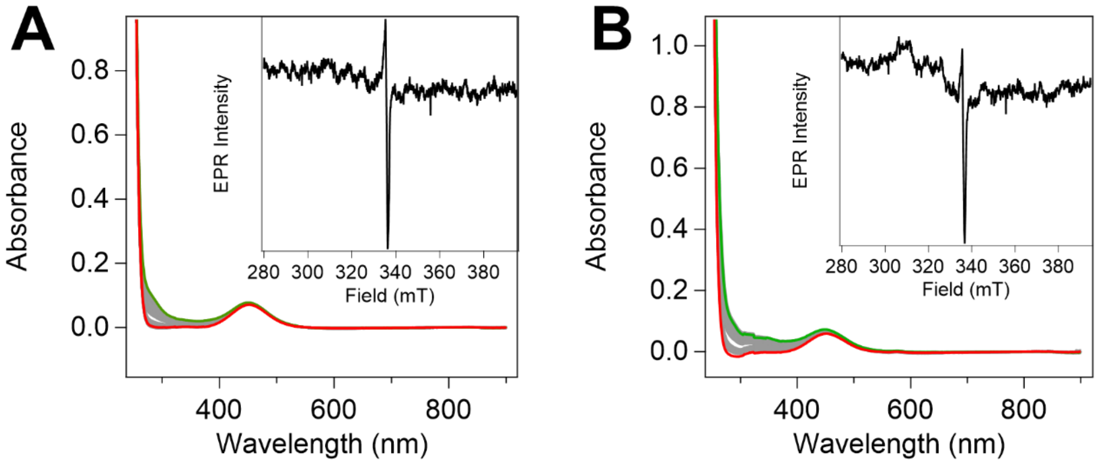

Figure S29. Spectroelectrochemistry of [1] in different buffers. Optical spectroelectrochemistry of [**1**] under CO_2 with 0.1 M $NaClO_4$ in (A) 50 mM MOPS and (B) 50 mM PIPES buffers, pH 7.0. Samples were electrolyzed at -1.3 V vs NHE using an amorphous graphite rod as a working electrode. Spectra highlighted were taken at t = 1 min (red) and t = 60 min (green). (*Inset*) EPR spectra of the indicated samples following electrolysis.

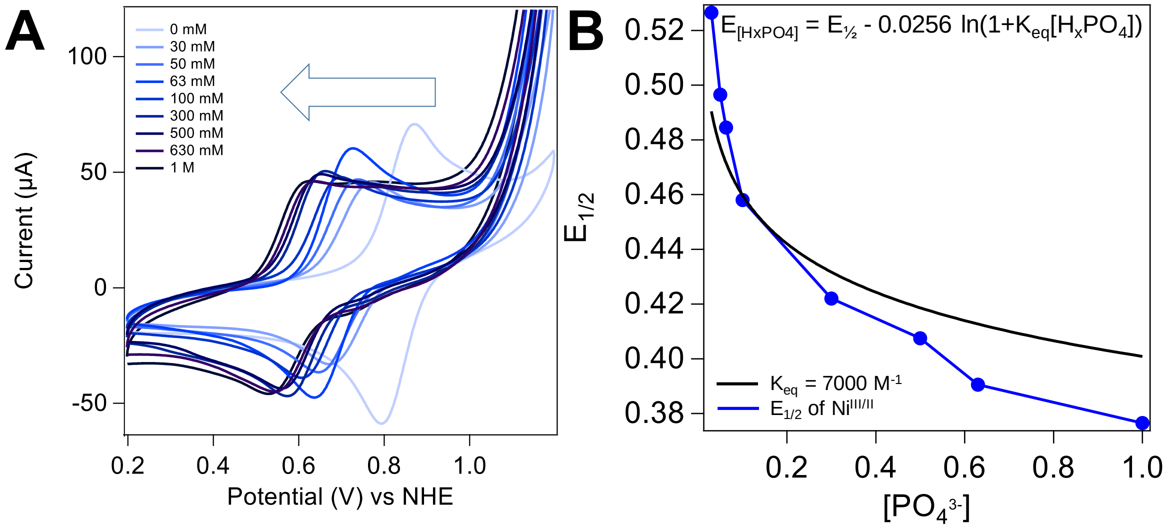

Figure S30. Cyclic voltammograms (CVs) with varying amounts of phosphate. (A) CVs of [**1**] under an atmosphere of CO_2 (blue) (ν = 10 mV/s). CVs were run with an amorphous graphite working electrode and varying concentrations of phosphate buffer (as indicated), pH 7.0, with 0.1 M KCl. (B) Nernstian fit (black) to the $E_{1/2}$ values (blue) measured as a function of the phosphate concentration. Equation used for extracting the binding constant given in figure.

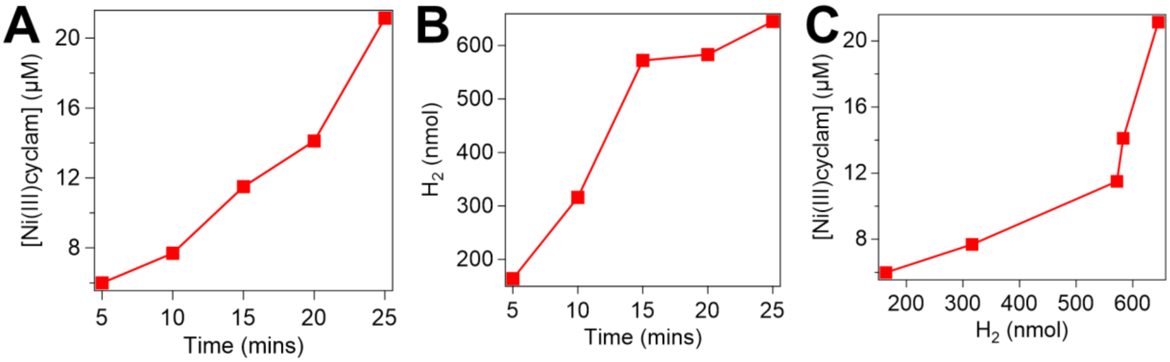

Figure S31. Correlation between Ni^{III} species generated and H_2 produced as a function of time under an atmosphere of CO. Electrolysis was performed at -1.3 V (vs. NHE) using an AG rod working electrode. Samples were prepared in 50 mM phosphate buffer, pH 7.0, under a CO atmosphere. (A) EPR spin quantitation of $[Ni(cyclam)]^{3+}$ generated and (B) hydrogen produced as a function of time during electrolysis. (C) Correlation between $[Ni(cyclam)]^{3+}$ and H_2 generated during electrolysis under CO.

		Bond Lengths (Å)				
		Ni- N_1	Ni- N_2	Ni- N_3	Ni- N_4	Ni- X (x= H_2O, OH^-, Cl^-, H^-, or $H_XPO_4^{n-}$)
Ni^I	**Trans I**	2.078	2.087	2.076	2.087	---
	Trans III	2.081	2.084	2.082	2.084	---
Ni^{III}	**Trans I**	1.995	1.997	1.998	1.996	---
	Trans III	1.995	1.998	1.995	1.998	---
	Trans III + H_2O	2.002	1.999	1.993	1.993	2.150
	Trans III + $2H_2O$	1.991	1.993	1.991	1.993	2.296, 2.297
	Trans III + OH^-	1.976	1.978	1.974	1.976	1.938
	Trans III + Cl^-	1.982	1.979	1.978	1.978	2.300
	Trans III + $2Cl^-$	1.981	1.985	1.981	1.986	2.422, 2.420
	Trans III + H^-	2.061	1.942	2.062	1.956	1.520
	Trans III + PO_4^{3-}	2.047	2.095	2.117	2.085	1.947
	Trans III + HPO_4^{2-}	1.963	1.971	1.983	1.977	2.521
	Trans III + $H_2PO_4^-$	1.980	1.993	1.974	1.974	1.968
	Trans III + H_3PO_4	1.993	1.990	1.986	1.986	2.040
	Trans III + $2HPO_4^{2-}$	2.169	1.974	2.157	1.957	1.905, 1.915
	Trans III + $2H_2PO_4^-$	1.987	1.990	1.973	1.971	2.082, 2.125
	Trans III + $2H_3PO_4$	1.983	1.990	1.980	1.985	2.197, 2.174

Table ST4. **Bond lengths of select [Ni(cyclam)] models**. Bond lengths obtained from energy-minimized DFT structures (def2-TZVPP basis set, B3LYP functional).

		g_1	g_2	g_3	g_{iso}
	Experimental	2.023	2.173	2.210	2.13
Ni^I	**Trans I**	2.061	2.064	2.19	2.105
	Trans III	2.058	2.061	2.181	2.100
Ni^{III}	**Trans I**	2.041	2.433	2.441	2.305
	Trans III	2.039	2.422	2.430	2.297
	Trans III + H_2O	2.041	2.267	2.277	2.195
	Trans III + $2H_2O$	2.039	2.223	2.224	2.162
	Trans III + OH^-	2.027	2.115	2.116	2.086
	Trans III + Cl^-	2.027	2.128	2.129	2.095
	Trans III + $2Cl^-$	2.026	2.104	2.106	2.079
	Trans III + H^-	2.004	2.053	2.105	2.054
	Trans III + PO_4^{3-}	1.828	2.002	2.205	2.012
	Trans III + HPO_4^{2-}	1.921	2.007	2.100	2.009
	Trans III + $H_2PO_4^-$	2.033	2.176	2.177	2.129
	Trans III + H_3PO_4	2.039	2.248	2.251	2.179
	Trans III + $2HPO_4^{2-}$	2.036	2.098	2.143	2.093
	Trans III + $2H_2PO_4^-$	2.032	2.144	2.146	2.107
	Trans III + $2H_3PO_4$	2.036	2.192	2.193	2.141

Table ST5. **Calculated *g*-values for possible [Ni(cyclam)] models**. *g*-values calculated from the energy-minimized structures using the B3LYP functional.

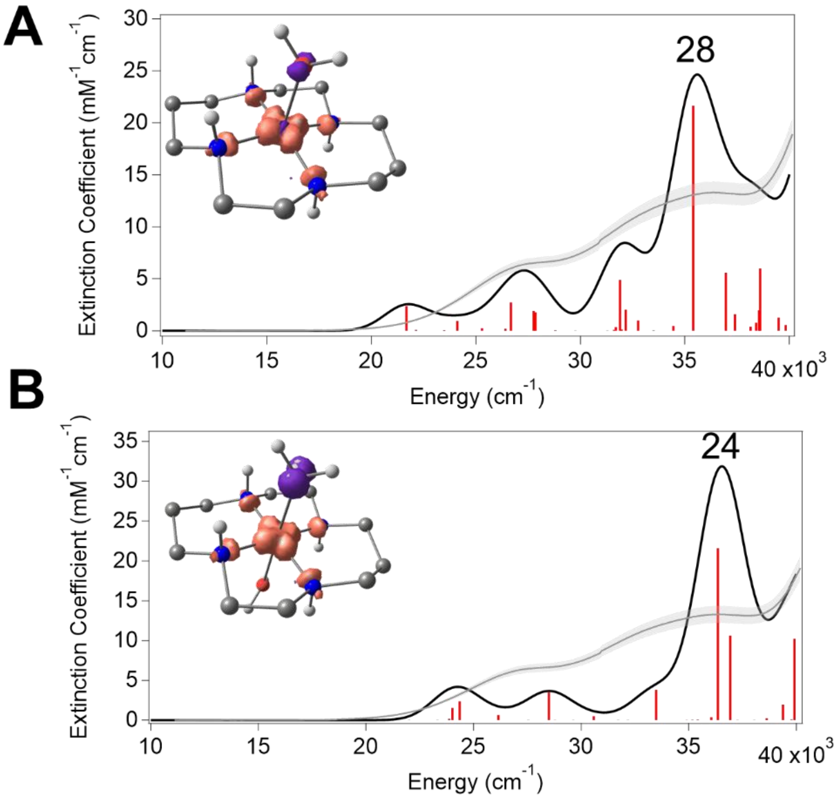

Figure S32. TD-DFT calculated absorption spectra of hydrated [Ni(cyclam)(H_2O)$_x$]$^{3+}$ in the trans-III conformation. (A) Time-dependent DFT (TD-DFT) transitions (red sticks) and calculated spectrum (black) of a singly hydrated model (x = 1) overlaid with experimental data (grey). (*Inset*) Difference density shown for State 28, which was selected for the RR calculations shown in Figure S38. (B) TD-DFT transitions (red sticks) and calculated spectrum (black) of a doubly hydrated model (x = 2) overlaid with experimental data (grey). (*Inset*) Difference density shown for State 24, which was selected for the RR calculations shown in Figure S38. Positive difference density is shown in pink, and negative difference density is shown in purple.

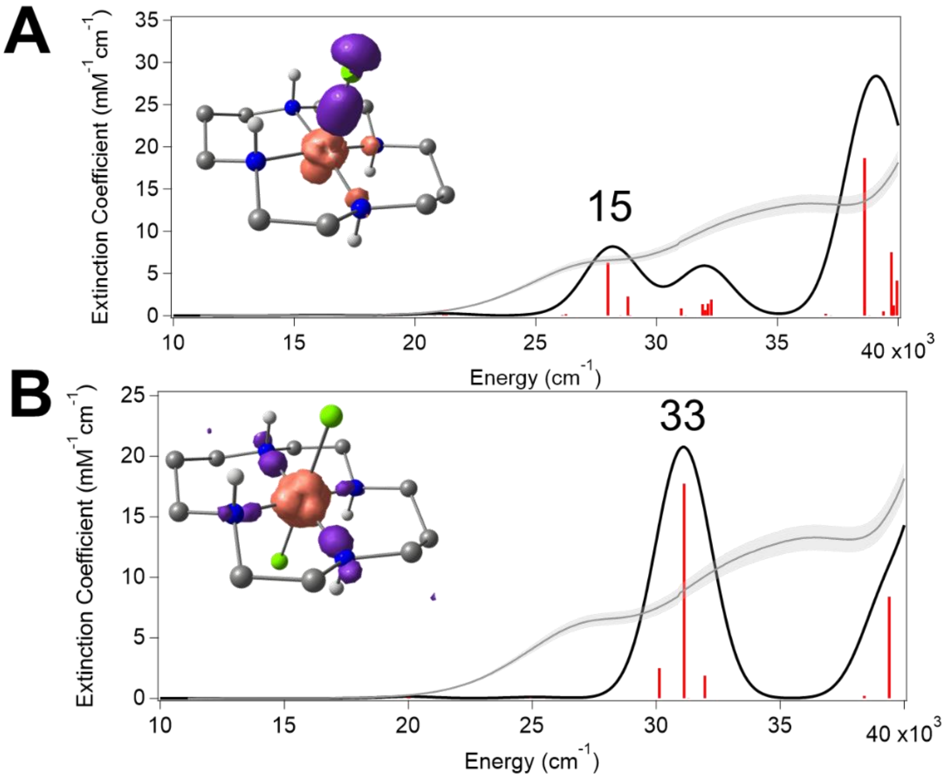

Figure S33. TD-DFT calculated absorption spectra of chlorinated [Ni(cyclam)Cl$_x$]$^{3+}$ models in the trans-III conformation. (A) Time-dependent DFT (TD-DFT) transitions (red sticks) and calculated spectrum (black) of a model with a single chloride ligand (x = 1) overlaid with experimental data (grey). (*Inset*) Difference density shown for State 15, which was selected for the RR calculations shown in Figure S38. (B) TD-DFT transitions (red sticks) and calculated spectrum (black) of a model with two chloride ligands (x = 2) overlaid with experimental data (grey). (*Inset*) Difference density shown for State 33, which was selected for the RR calculations shown in Figure S38. Positive difference density is shown in pink, and negative difference density is shown in purple.

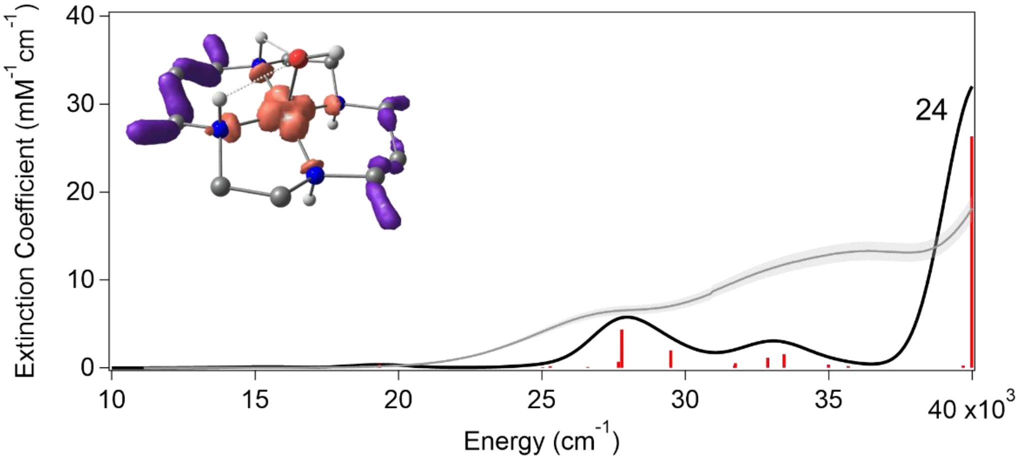

Figure S34. TD-DFT calculated absorption spectrum of [Ni(cyclam)(OH)]$^{2+}$ in the trans-III conformation. (A) Time-dependent DFT (TD-DFT) transitions (red sticks) and calculated spectrum (black) of [Ni(cyclam)(OH)]$^{2+}$ overlaid with experimental data (grey). (*Inset*) Difference density shown for State 24, which was selected for the RR calculations shown in Figure S38.

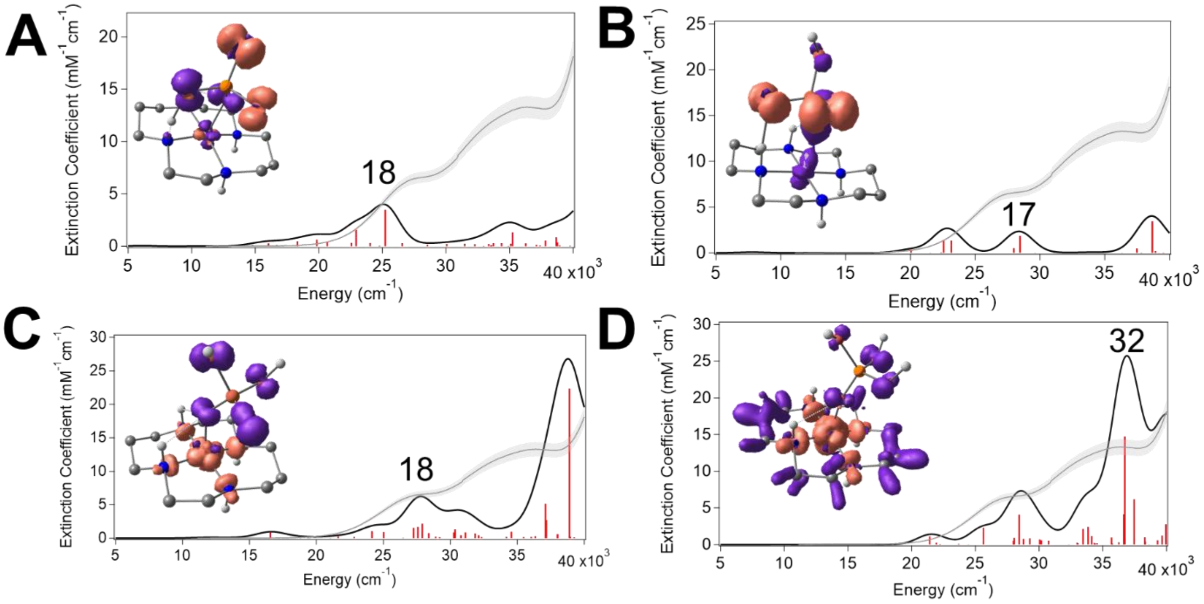

Figure S35. TD-DFT calculated absorption spectra of [Ni(cyclam)(H_xPO_4)]$^{x+}$ in the trans-III conformation. (A) Time-dependent DFT (TD-DFT) transitions (red sticks) and calculated spectrum (black) of Ni(cyclam)(PO_4) (x = 0) overlaid with experimental data (grey). (*Inset*) Difference density shown for State 18, which was selected for the RR calculations shown in Figure S39. (B) Time-dependent DFT (TD-DFT) transitions (red sticks) and calculated spectrum (black) of [Ni(cyclam)(HPO_4)]$^{+}$ (x = 1) overlaid with experimental data (grey). (*Inset*) Difference density shown for State 17, which was selected for the RR calculations shown in Figure S39. (C) Time-dependent DFT (TD-DFT) transitions (red sticks) and calculated spectrum (black) of [Ni(cyclam)(H_2PO_4)]$^{2+}$ (x = 2) overlaid with experimental data (grey). (*Inset*) Difference density shown for State 18, which was selected for the RR calculations shown in Figure S39. (D) Time-dependent DFT (TD-DFT) transitions (red sticks) and calculated spectrum (black) of [Ni(cyclam)(H_3PO_4)]$^{3+}$ (x = 3) overlaid with experimental data (grey). (*Inset*) Difference density shown for State 32, which was selected for the RR calculations shown in Figure S39.

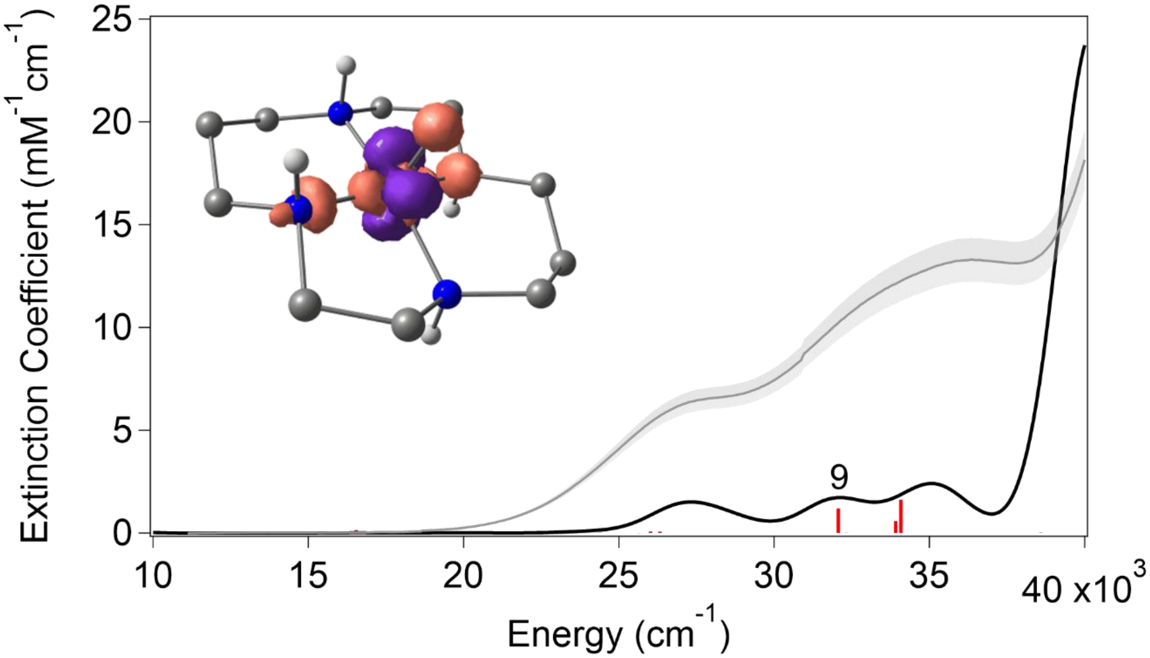

Figure S36. TD-DFT calculated absorption spectrum of $[Ni(cyclam)(H)]^{2+}$ in the trans-III conformation. (A) Time-dependent DFT (TD-DFT) transitions (red sticks) and calculated spectrum (black) of the hydride-bound model overlaid with experimental data (grey). (*Inset*) Difference density shown for State 9, which was selected for the RR calculations shown in Figure S38.

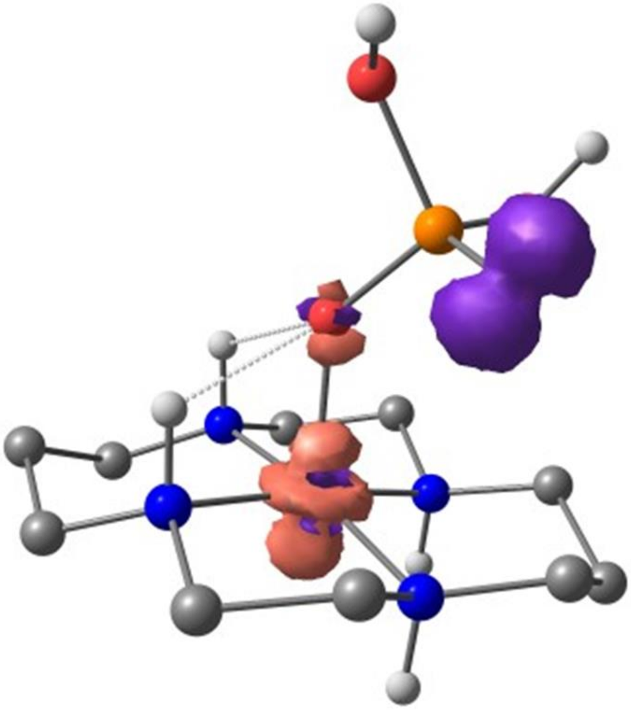

Figure S37. Electronic transition difference density for State 5 of [Ni(cyclam)(H_2PO_4)]$^{2+}$. Structure of [Ni(cyclam)(H_2PO_4)]$^{2+}$ shown with transition difference density (positive density shown in pink, negative density shown in purple) for State 5, which is calculated to occur at 16,563 cm^{-1} (Figure 3A).

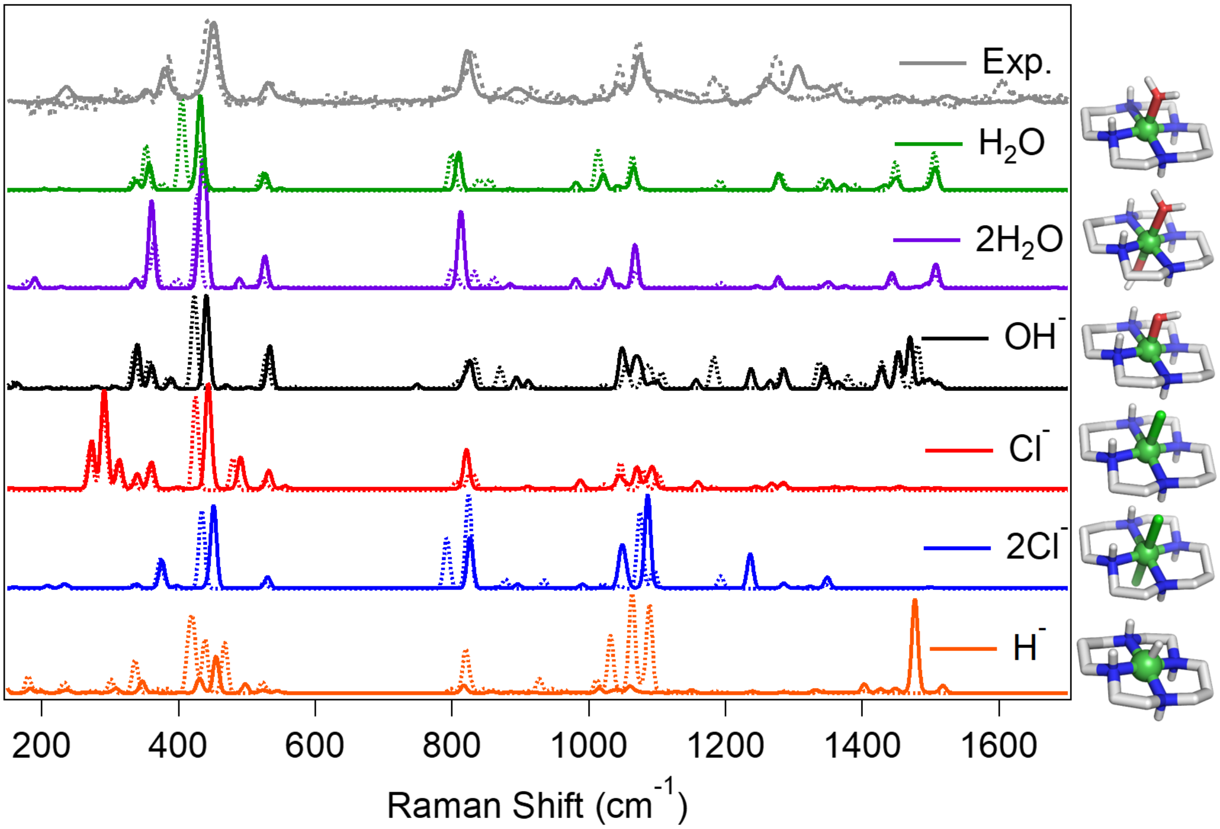

Figure S38. Calculated resonance Raman spectra for [Ni(cyclam)] models compared to experimental data. Calculated resonance Raman spectra for [Ni^{III}(cyclam)] in the trans-III conformation with one H_2O ligand bound (green), two H_2O ligands bound (purple), one OH$^-$ ligand bound (black), one Cl$^-$ ligand bound (red), two Cl$^-$ ligands bound (blue), or one H$^-$ ligand bound (orange). Spectra for protonated compounds (modeling samples prepared in H_2O) shown as solid lines and deuterated compounds (modeling samples prepared in D_2O) overlaid in dotted lines. Calculated spectra were convolved with a 10 cm^{-1} linewidth using an excitation energy of 35,000 cm^{-1} for the hydrated and hydride models, 30,000 cm^{-1} for the singly chlorinated model, and 40,000 cm^{-1} for the doubly chlorinated and the hydroxide models. (*Right*) Structures of each model.

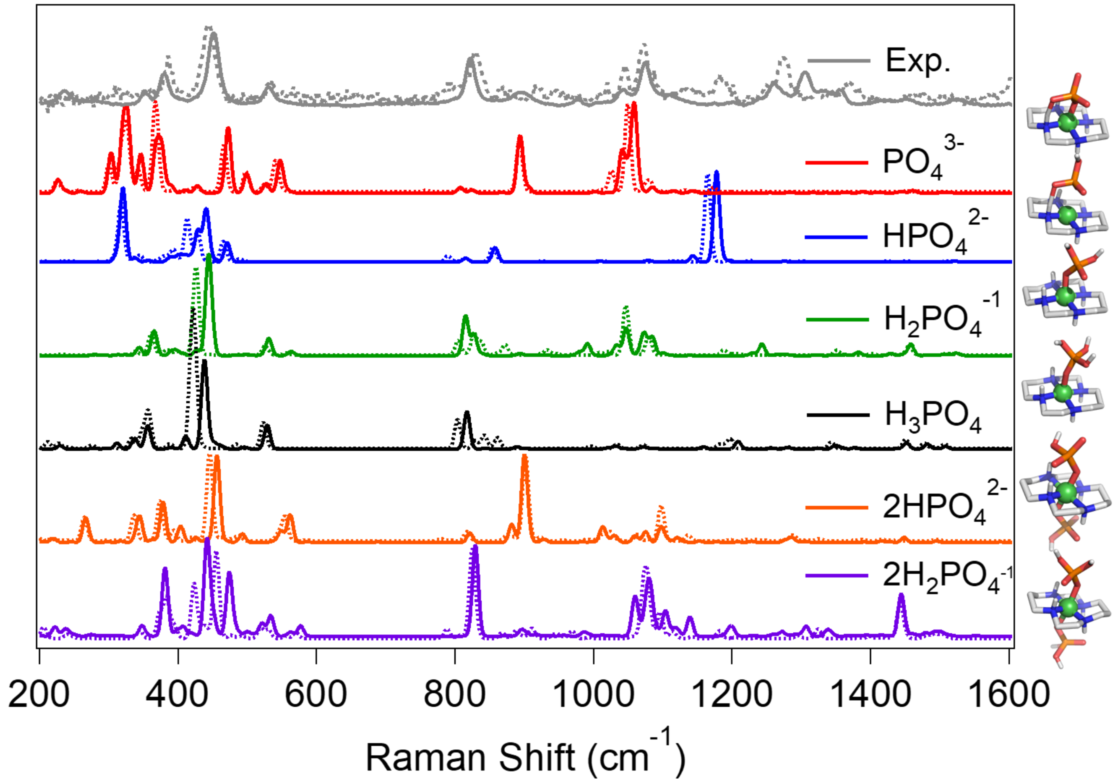

Figure S39. Calculated resonance Raman spectra of phosphate-bound [Ni(cyclam)] models compared to experimental data. Calculated resonance Raman spectra for [Ni^{III}(cyclam)] in the trans-III conformation with phosphate ligands bound in varying protonation states, as labeled and with corresponding structures shown on the right-hand side. Spectra for protonated compounds (modeling samples prepared in H_2O) shown as solid lines and deuterated compounds (modeling samples prepared in D_2O) overlaid in dotted lines. Calculated spectra were convolved with a 10 cm^{-1} linewidth using excitation energies between 27,000 and 40,000 cm^{-1}.

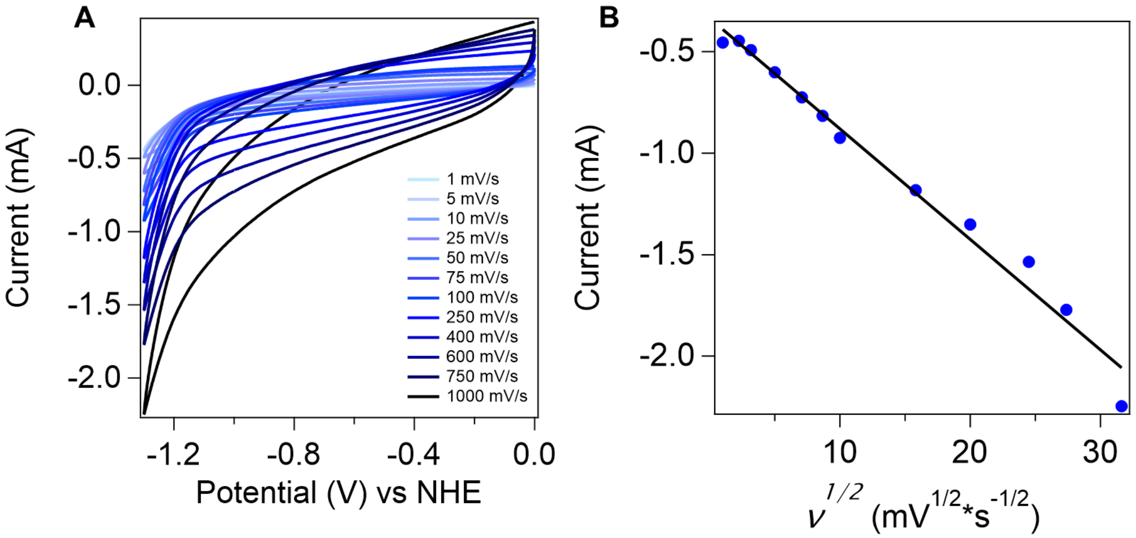

Figure S40. Scan rate dependence of catalytic currents of [1]. (A) Cyclic voltammograms (CVs) of 1.2 mM [**1**] in 50 mM phosphate buffer, pH 7.0, with 0.1 M KCl under a CO_2 atmosphere measured with varying scan rates, as indicated. CVs were run with an amorphous graphite working electrode. (B) Maximum catalytic currents at -1.3 V vs NHE (blue) and linear fit (black) shown as a function of the square root of the scan rate ($\nu^{1/2}$).